J. Fluid Mech. (2022), *vol*. 932, A47, doi:10.1017/jfm.2021.1001

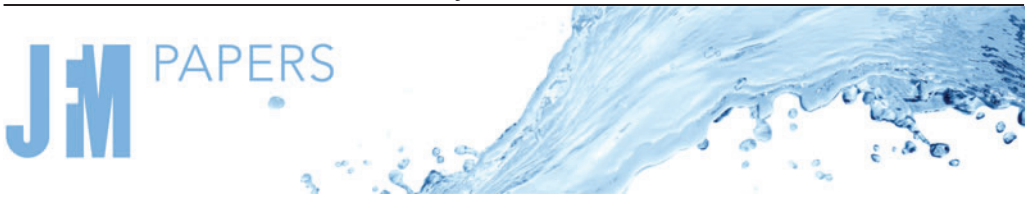

Under pressure: turbulent plumes in a uniform crossflow

Owen H. Jordan[1], **Gabriel G. Rooney**[2], **Benjamin J. Devenish**[2] and **Maarten van Reeuwijk**[1],†

[1]Department of Civil and Environmental Engineering, Imperial College London, London SW7 2AZ, UK

[2]Met Office, FitzRoy Road, Exeter EX1 3PB, UK

(Received 31 July 2020; revised 8 October 2021; accepted 4 November 2021)

Direct numerical simulation is used to investigate the integral behaviour of buoyant plumes subjected to a uniform crossflow that are infinitely lazy at the source. Neither a plume trajectory defined by the centre of mass of the plume z_c nor a trajectory defined by the central streamline z_U is aligned with the average streamlines inside the plume. Both z_c and z_U are shown to correlate with field lines of the total buoyancy flux, which implies that a model for the vertical turbulent buoyancy flux is required to faithfully predict the plume angle. A study of the volume conservation equation shows that entrainment due to incorporation of ambient fluid with non-zero velocity due to the increase in the surface area (the Leibniz term) is the dominant entrainment mechanism in strong crossflows. The data indicate that pressure differences between the top and bottom of the plume play a leading role in the evolution of the horizontal and vertical momentum balances and are crucial for appropriately modelling plume rise. By direct parameterisation of the vertical buoyancy flux, the entrainment and the pressure, an integral plume model is developed which is in good agreement with the simulations for sufficiently strong crossflow. A perturbation expansion shows that the current model is an intermediate-range model valid for downstream distances up to $100\ell_b$–$1000\ell_b$, where ℓ_b is the buoyancy length scale based on the flow speed and plume buoyancy flux.

Key words: plumes/thermals, turbulent mixing

1. Introduction

Turbulent buoyant plumes have long been studied due to their ubiquity in nature and in industry, and their importance in fields such as disaster management and industrial pollution. Examples are volcanic eruptions, pollutant dispersion via chimneys, fires, ocean outfalls and jet engines (Woods 2010; Mahesh 2013). A significant number of parameters

† Email address for correspondence: m.vanreeuwijk@imperial.ac.uk

play a role in the evolution of a buoyant plume. These include the source velocity, release angle, density and the state of the atmosphere the plume ascends through via the velocity profile $\boldsymbol{U}(z)$ and the stratification, characterised by the (square) buoyancy frequency $N^2(z)$. Volcanic applications feature another level of complexity due to the initial ash volume fraction and its size distribution, ash reactivity and compressibility effects including shock waves due to supersonic conditions at the source.

Buoyant plumes are typically modelled via integral models. The now-classical plume equations were presented in Morton, Taylor & Turner (1956), and comprise a set of three coupled ordinary differential equations for the volume flux Q, (streamwise) momentum flux M and buoyancy flux F, respectively. This theory was formulated in the absence of a crossflow such that the plume only evolves in the vertical coordinate z. One of the cornerstones of the theory is the entrainment assumption, which links the entrainment of fluid into the plume to the characteristic velocity inside the plume. Morton *et al.* (1956) assumed that the entrainment coefficient α was constant, although different values of α are typically used for jets and plumes. Recent work by van Reeuwijk & Craske (2015) has clarified the relation between the Morton *et al.* (1956) model and the Priestley & Ball (1955) model, who used a closure involving the production of turbulent kinetic energy. Analysis of experimental and numerical data by van Reeuwijk & Craske (2015) indicated that for jets and plumes the more suitable model is that of Priestley & Ball. In fully self-similar conditions, and with the buoyancy and velocity profiles having an equal width (List 1982), it follows directly that $\alpha_{plume} \approx (5/3)\alpha_{jet}$ (van Reeuwijk *et al.* 2016).

Integral plume models were extended to crossflows by, for example, Briggs (1982) and Weil (1988) and references therein: for strongly bent-over plumes they showed that analytical expressions could be derived for the level of neutral buoyancy and the maximum rise height of the plume. This involved adding an ordinary differential equation for the horizontal momentum excess flux M_x. The presence of a crossflow fundamentally alters the entrainment properties of a plume: it typically causes the flow to bend over and organise itself into a double-roll structure with two turbulent counter-rotating vortices (Fischer *et al.* 1979; Weil 1988; Huq & Dhanak 1996). For jets in a crossflow, Mahesh (2013) summarises the research of the double-roll structure and describes the horseshoe and wake vortices which form upstream of the jet's leading edge as a result of adverse pressure gradients.

In parallel with the effort to develop a suitable integral plume model, there is a large body of literature documenting experimental and numerical surveys of plumes in a crossflow (e.g. Cintolesi, Petronio & Armenio 2019). One of the earliest experimental studies (Fan 1967) investigates two categories of plumes: inclined plumes discharged into a stratified but quiescent environment, and plumes discharged into a homogeneous, uniform crossflow. Subsequent studies have been carried out for a wide range of initial and boundary conditions, resulting in a large catalogue of experimental work. For example, Gaskin (1995) compares a plume in a quiescent environment to a plume with a uniform crossflow, and Huq & Stewart (1996) assess the effects of atmospheric turbulence on plume development. With the increasingly widespread availability of high-powered computing, numerical studies and particularly large-eddy simulations (LES) have become an additional powerful tool for investigating plume dynamics. Yuan, Street & Ferziger (1999) were early innovators in this regard, simulating jets in a crossflow (without buoyancy) by utilising a dynamic Smagorinsky model for the subgrid scales. They used their LES to analyse the counter-rotating vortex structure, concluding that it was the result of the hanging vortices which appear in the region close to the source of the jet. More recently, De Wit, Van Rhee & Keetels (2014) examined a real-world application of LES to overflow dredging plumes resulting from a moving dredger. They discovered that the average horizontal velocity of the plume exceeds the speed of the crossflow. We discuss

this intriguing phenomenon in §§ 6 and 7. Another pertinent numerical study is that of Devenish *et al.* (2010) presenting LES of purely buoyant plumes released into stratified and uniform environments. They compared the results of their LES with plume integral models and proposed a modified entrainment assumption in which the contributions from the horizontal and vertical velocity components are not equally weighted.

There are various entrainment assumptions (see § 5), and all involve some mix of the plume velocity and the crossflow speed. Most models assume that the pressure is hydrostatic within the plume at least when averaged over the plume cross-section, and that the effects of pressure can be represented by an added-mass coefficient. Most models also neglect the Leibniz term: the increase in (for example) integral volume flux as a result of the spreading of the plume into a non-quiescent atmosphere. Schatzmann (1978), on the other hand, fully integrated the governing equations and was the first to describe an integral plume model incorporating the Leibniz term. He argued that this term should not be counted towards entrainment, since it requires a fundamentally different interpretation of the entrainment coefficient. In addition, he noted the need for a pressure term, although at the time not enough was known to fully model it. Limitations of his analysis are the assumption of axisymmetry and the assumption that the turbulence terms are negligible. We avoid these assumptions in our analysis by integrating the Reynolds-averaged equations directly, allowing us to assess all terms in the integral budgets and to determine which are physically relevant and which can be ignored.

One pertinent example of an application in which integral models play a key role is in the determination of the mass flux of a volcanic eruption. It is not possible to measure this quantity directly, so the mass flux is often inferred from the rise height of the plume, which is where the plume has the same density as the surrounding atmosphere and starts spreading laterally like a gravity current. Turbulent entrainment thus plays a key role in the rise height, since this is the sole mechanism by which the plume dilutes. Appropriately incorporating the influence of crossflow in these estimates is key for appropriate estimation of the source mass flux (Devenish 2013; Woodhouse *et al.* 2013; Costa *et al.* 2016; Rossi, Bonadonna & Degruyter 2019).

The aim of this paper is to examine the assumptions underlying integral models of plumes in a crossflow, including entrainment, by means of direct numerical simulation (DNS). In order to manage the complexity of the problem, we restrict ourselves to a neutral atmosphere ($N = 0$) with a uniform crossflow speed U and a momentumless source (i.e. an infinitely lazy plume). The only parameter that is varied is the crossflow speed. We focus our attention on the behaviour exhibited by plumes with a strong crossflow, and on developing a model for the entrainment and pressure drop over the plume.

2. Theory

2.1. *Integral equations*

In this section, equations for the integral volume, momentum and buoyancy fluxes are derived. The derivation is consistent with that of Weil (1988) and Schatzmann (1978), but is performed here without any simplifications, such as the assumption of axisymmetry (Schatzmann 1978) or neglecting turbulence and pressure terms. A schematic detailing the nomenclature used here is given in figure 1. Cartesian coordinates (x, y, z) are used which represent the streamwise, transverse and vertical directions, respectively. The crossflow speed in the x direction is denoted U and is uniform in z. It is convenient to also introduce a plume-following coordinate system (s, y, η), where s is the distance from the source along the plume centreline, y is the transverse direction (which remains unchanged) and

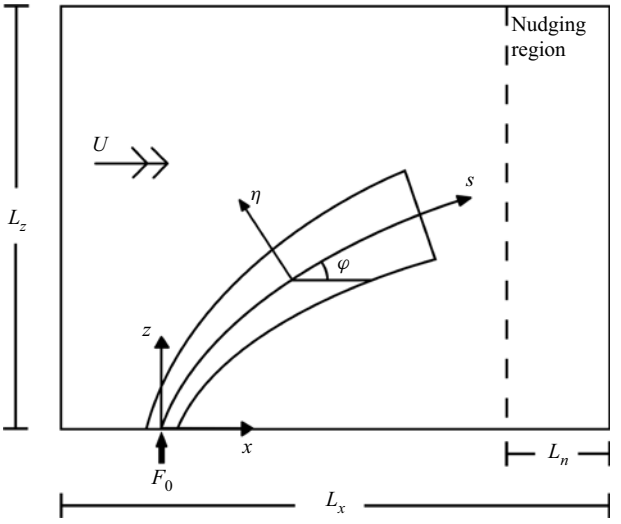

Figure 1. A schematic of the plume with the Cartesian (x, z) coordinate system and the curvilinear (s, η) coordinate system. The y direction is perpendicular to this plane. Values for L_x, L_z and L_n for the five simulations can be found in table 1.

η is the coordinate perpendicular to s in the (x, z) plane. The plume centreline makes an angle φ with the x axis. The plume source is positioned at (0, 0, 0) and the release is momentumless with a constant integral buoyancy flux $F_0 = r_0^2 \phi_b$, where r_0 is the source radius and ϕ_b is the (diffusive) buoyancy flux. This infinitely lazy plume condition is chosen so as not to introduce a further parameter, namely the source momentum flux, and to manage the complexity of the problem.

The incompressible Navier–Stokes equations with the Boussinesq approximation are

$$\nabla \cdot \boldsymbol{u} = 0, \tag{2.1a}$$

$$\frac{\partial \boldsymbol{u}}{\partial t} + \boldsymbol{u} \cdot \nabla \boldsymbol{u} = -\nabla p + \nu \nabla^2 \boldsymbol{u} + b\hat{\boldsymbol{k}}, \tag{2.1b}$$

$$\frac{\partial b}{\partial t} + \boldsymbol{u} \cdot \nabla b = \kappa \nabla^2 b, \tag{2.1c}$$

where $\boldsymbol{u} = (u, v, w)$ is the velocity of the fluid, $b = g(\rho_0 - \rho)/\rho_0$ is the buoyancy and $p = \tilde{p}/\rho_0 + gz$ is the kinematic pressure perturbation, where g is the gravitational acceleration, ρ_0 is a constant reference density and $\tilde{p}$ is the standard pressure. The kinematic viscosity and scalar diffusivity are denoted by ν and κ, respectively. Assuming high-Reynolds-number and high-Péclet-number flow, applying Reynolds averaging to (2.1) and making use of the fact that the flow is statistically steady results in

$$\nabla \cdot \bar{\boldsymbol{u}} = 0, \tag{2.2a}$$

$$\nabla \cdot (\bar{\boldsymbol{u}}\overline{u_i} + \overline{\boldsymbol{u}' u_i'}) = -\frac{\partial \bar{p}}{\partial x_i} + \bar{b}\delta_{i3}, \tag{2.2b}$$

$$\nabla \cdot (\bar{\boldsymbol{u}}\bar{b} + \overline{\boldsymbol{u}' b'}) = 0, \tag{2.2c}$$

where the overbars denote time averaging and fluctuating quantities are defined as $\phi' = \phi - \bar{\phi}$ for any variable ϕ.

Using that $\overline{\boldsymbol{u}}\bar{\phi} + \overline{\boldsymbol{u}'\phi'} = \overline{\boldsymbol{u}\phi}$, the equations above are all of the form (e.g. Weil 1988)

$$\boldsymbol{\nabla} \cdot \left(\overline{\boldsymbol{u}\phi}\right) = G, \tag{2.3}$$

which can be integrated over the plume cross-section A, whose domain is denoted Ω, to obtain (van Reeuwijk, Vassilicos & Craske 2021) (see Appendix A)

$$\frac{\mathrm{d}}{\mathrm{d}s}\iint_{\Omega} \bar{u}_s\bar{\phi} + \overline{u_s'\phi'}\,\mathrm{d}A = \iint_{\Omega} G\,\mathrm{d}A + \pi E[\phi] + \pi\mathcal{L}[\phi], \tag{2.4}$$

where $\bar{u}_s = \bar{u}\cos\varphi + \bar{w}\sin\varphi$ is the mean velocity in the s direction and $\Omega(s)$ represents the domain occupied by the plume. See § 3.2 for a description of how Ω is determined practically. In deriving the equation above it was assumed that the curvature of the plume trajectory $\mathrm{d}\varphi/\mathrm{d}s \ll 1$ (see Appendix A for more details). The boundary terms $E[\phi]$ and $\mathcal{L}[\phi]$ are line integrals of the form

$$E[\phi] = \frac{1}{\pi}\oint_{\partial\Omega} \overline{\boldsymbol{u}_\perp\phi}\cdot\boldsymbol{n}\,\mathrm{d}\ell, \quad \mathcal{L}[\phi] = \frac{1}{\pi}\oint_{\partial\Omega} \overline{u_s\phi}\frac{N_s}{|\boldsymbol{N}_\perp|}\,\mathrm{d}\ell, \tag{2.5a,b}$$

where $\partial\Omega$ denotes the plume boundary, $\boldsymbol{N} = (N_s, N_y, N_\eta)^{\mathrm{T}}$ denotes the three-dimensional inward-pointing normal along $\partial\Omega$, $\boldsymbol{N}_\perp = (N_y, N_\eta)^{\mathrm{T}}$ and $\boldsymbol{u}_\perp = (u_y, u_\eta)^{\mathrm{T}}$ are the vector components in the (y, η) plane and $\boldsymbol{n} = \boldsymbol{N}_\perp/|\boldsymbol{N}_\perp|$ is the inward-pointing two-dimensional normal in the (y, η) plane. As the plume boundary will be detected via the average buoyancy field $\bar{b}$ (see § 4), $\boldsymbol{N}$ is defined as $\boldsymbol{N} = \boldsymbol{\nabla}\bar{b}/|\boldsymbol{\nabla}\bar{b}|$ (see also van Reeuwijk *et al.* 2021). The factor $1/\pi$ in the definition of $\mathcal{L}[\phi]$ and $E[\phi]$ is introduced for consistency with the convention in plume theory of dividing the integral quantities through by π (see (2.7)).

The terms $E[\phi]$ and $\mathcal{L}[\phi]$ represent distinct physical processes by which the quantity ϕ enters the plume. The term $E[\phi]$ represents the advection of ϕ into the plume; the term $\mathcal{L}[\phi]$ represents incorporation of the quantity ϕ via expansion of the plume into a non-quiescent atmosphere – if the plume surface area A over which the governing equations are integrated changes as a function of s, and the value of ϕ at the boundary of the plume is non-zero, then the surface integral will be increased by a quantity equal to $[\overline{u_s\phi}]_b\,\mathrm{d}A/\mathrm{d}s$, where $[\overline{u_s\phi}]_b$ is the average value of $\overline{u_s\phi}$ at the boundary.

Integrating the Navier–Stokes equations over the plume cross-section and applying (2.4) with $\phi = 1, u - U, w$ and b, respectively, results in

$$\frac{\mathrm{d}Q}{\mathrm{d}s} = E[1] + \mathcal{L}[1] = E + \mathcal{L}, \tag{2.6a}$$

$$\frac{\mathrm{d}M_x}{\mathrm{d}s} + \frac{\mathrm{d}M_x'}{\mathrm{d}s} = -P_x + E[u-U] + \mathcal{L}[u-U], \tag{2.6b}$$

$$\frac{\mathrm{d}M_z}{\mathrm{d}s} + \frac{\mathrm{d}M_z'}{\mathrm{d}s} = -P_z + B + E[w] + \mathcal{L}[w], \tag{2.6c}$$

$$\frac{\mathrm{d}F}{\mathrm{d}s} + \frac{\mathrm{d}F'}{\mathrm{d}s} = E[b] + \mathcal{L}[b], \tag{2.6d}$$

where the integral volume flux Q, the horizontal momentum excess flux M_x, the vertical momentum flux M_z, the buoyancy flux F and the integral horizontal and vertical pressures

P_x and P_z are defined as

$$\left.\begin{aligned} Q &= \frac{1}{\pi}\iint_{\Omega} \bar{u}_s \,\mathrm{d}A, & F &= \frac{1}{\pi}\iint_{\Omega} \bar{u}_s \bar{b} \,\mathrm{d}A, \\ M_x &= \frac{1}{\pi}\iint_{\Omega} \bar{u}_s(\bar{u}-U) \,\mathrm{d}A, & P_x &= \frac{1}{\pi}\iint_{\Omega} \frac{\partial \bar{p}}{\partial x} \,\mathrm{d}A, \\ M_z &= \frac{1}{\pi}\iint_{\Omega} \bar{u}_s \bar{w} \mathrm{d}A, & P_z &= \frac{1}{\pi}\iint_{\Omega} \frac{\partial \bar{p}}{\partial z} \,\mathrm{d}A, \\ M_x' &= \frac{1}{\pi}\iint_{\Omega} \overline{u_s' u'} \,\mathrm{d}A, & F' &= \frac{1}{\pi}\iint_{\Omega} \overline{u_s' b'} \,\mathrm{d}A, \\ M_z' &= \frac{1}{\pi}\iint_{\Omega} \overline{u_s' w'} \mathrm{d}A, & B &= \frac{1}{\pi}\iint_{\Omega} \bar{b} \,\mathrm{d}A. \end{aligned}\right\} \tag{2.7}$$

The scalar $\bar{u} - U$ is chosen for the x-momentum equation so as to be consistent with the work of Weil (1988) in the definition of M_x. The integral therefore represents the momentum flux in the x direction in excess of the x-momentum flux of the ambient atmosphere. A consequence of this choice of variable is that the Leibniz and entrainment terms for the x-momentum equation are significantly reduced, due to the fact that to first order $u \approx U$ at the boundary of the plume.

2.2. *Plume models*

In conventional plume theory $\bar{u} - U$, $\bar{w}$ and $\bar{b}$ are assumed to vanish at the plume boundary. In addition $\mathcal{L}[1]$ is assumed to be small. It thus follows that all entrainment and Leibniz terms are negligible except for $E \equiv E[1]$. Furthermore, it is commonly assumed that the pressure at the plume boundary is equal to the ambient pressure, which implies that P_x and P_z are zero (although vertical pressure gradients are taken into account implicitly via an added-mass coefficient). The buoyancy integral $B = \pi^{-1}\int \bar{b}\mathrm{d}A$ is generally modelled as $B = F/U_s$ (Weil 1988), where U_s is the characteristic velocity of the plume, defined as

$$U_s = (U + u_m)\cos\varphi + w_m \sin\varphi. \tag{2.8}$$

Here, u_m is is the characteristic horizontal plume velocity relative to the crossflow (horizontal velocity excess), w_m is the characteristic vertical velocity and φ is the angle of the plume. These characteristic quantities are linked to the integral quantities by

$$Q = r_m^2 U_s, \quad M_x = r_m^2 U_s u_m, \quad M_z = r_m^2 U_s w_m, \quad F = r_m^2 U_s b_m. \tag{2.9a–d}$$

Here, b_m is the characteristic buoyancy or reduced gravity and r_m is the characteristic plume radius. Equation (2.9*a–d*) implicitly provides the definition of u_m, w_m and b_m as M_x/Q, M_z/Q and F/Q, respectively. The characteristic radius r_m is defined as $r_m = (Q/U_s)^{1/2}$ (i.e. using the definition of Q; (2.9*a*)), which encapsulates both the pure plume definition $r_m = Q/M_z^{1/2}$ for $U \ll w_m$, $u_m \ll w_m$, and the bent-over solution $r_m = (Q/U)^{1/2}$ for $U \gg u_m$, $U \gg w_m$.

The entrainment term E is typically parameterised as (Weil 1988; Devenish *et al.* 2010)

$$E = 2\gamma r_m w_m, \tag{2.10}$$

where γ is the entrainment coefficient and r_m and w_m are a characteristic radius and vertical velocity, respectively. Invoking the assumptions stated at the start of this section

($\mathcal{L} \ll 1$ and $E \equiv E[1]$), neglecting turbulent fluxes and substituting (2.10) into the integral equations (2.6*a–d*) result in

$$\frac{\mathrm{d}Q}{\mathrm{d}s} = 2\gamma \frac{M_z}{r_m U_s}, \quad \frac{\mathrm{d}M_x}{\mathrm{d}s} = 0, \quad (1+k)\frac{\mathrm{d}M_z}{\mathrm{d}s} = \frac{F}{U_s}, \quad \frac{\mathrm{d}F}{\mathrm{d}s} = 0. \tag{2.11a–d}$$

Here k is the added-mass constant which takes into account the effects of an adverse pressure gradient on the vertical motion (e.g. Weil 1988), which compensates for the fact that no explicit integral pressure terms are present. It is introduced by analogy with the motion of a solid body and is equivalent to using a drag term (see Briggs 1982; Schatzmann 1978; Davidson 1989). Kinematic relations for the plume trajectory are required to evolve the plume in space:

$$\frac{\mathrm{d}x}{\mathrm{d}s} = \cos\varphi, \quad \frac{\mathrm{d}z}{\mathrm{d}s} = \sin\varphi. \tag{2.12a,b}$$

To close the set of equations, the plume angle φ is conventionally assumed to be the angle of the local streamlines φ_u, defined via

$$\tan\varphi_u = \frac{w_m}{U + u_m}. \tag{2.13}$$

Under the assumption that $\varphi = \varphi_u$, U_s represents the velocity magnitude $\sqrt{(U+u_m)^2+w_m^2}$, which can then be equivalently expressed in terms of the integral quantities as $Q^{-1}\sqrt{(QU+M_x)^2+M_z^2}$. Here, we make an explicit difference between φ and φ_u since it will turn out that these quantities are not identical for the flow cases under consideration (see § 4). When $\varphi \neq \varphi_u$, there is a component of velocity in the η direction:

$$U_\eta = -(U+u_m)\sin\varphi + w_m\cos\varphi. \tag{2.14}$$

2.3. *Bent-over plumes*

In this section we briefly provide an overview of analytical results for bent-over plumes in a neutral stratification and a uniform crossflow. Bent-over plumes are defined to have their centreline inclined at a very small angle to the horizontal (in which case the equations are formally equal to those for a line thermal; Briggs 1984; Lee & Chu 2003). This implies that $w_m \ll U$, $u_m \ll U$ and $\mathrm{d}s \approx \mathrm{d}x$. Assuming that in this case the entrainment rate is a constant, $\gamma = \beta'$, the following relations can be derived (e.g. Weil 1988). Integrating the volume flux equation (2.11*a*) yields

$$r_m = \beta' z_c + r_0, \tag{2.15}$$

where r_0 is the source radius. Integrating the vertical momentum flux equation (2.11*c*) twice and making use of (2.12*a*,*b*), (2.13) and (2.15), assuming $\varphi = \varphi_u$, results in

$$\frac{z_c}{\ell_b} = \left(\frac{3}{2\beta^2}\right)^{1/3}\left(\frac{x-x_v}{\ell_b}\right)^{2/3} \tag{2.16}$$

for $r_0 \ll \beta' z_c$, where $\ell_b = F/U^3$ is the buoyancy length scale and x_v is a virtual origin correction, which is a constant subtracted from the x coordinate of the plume trajectory that compensates for any near-field effects. It is necessary because the region close to the source (where $r_0 \ll \beta' z_c$ no longer holds) is not expected to obey the two-thirds law. The value of β is not equal to β', because of added-mass effects (Lee & Chu 2003), and

the two can be related as $\beta = \beta'\sqrt{1+k}$ (Weil 1988, p. 164; see also § 8), where k is the same added-mass coefficient as in (2.11*a–d*). Experiments indicate that $0.3 \lesssim k \lesssim 1.3$ (e.g. Briggs 1982; Weil 1988; Contini *et al.* 2011) and $0.45 \lesssim \beta' \lesssim 0.75$ (e.g. Hewett, Fay & Hoult 1971; Hoult & Weil 1972; Briggs 1984; Weil 1988; Huq & Stewart 1996). Although β' is a constant coefficient, it may vary between simulations or experiments dependent on factors such as the strength of the crossflow and the initial buoyancy flux F_0 (Briggs 1984).

Several entrainment models are in use for plumes in a crossflow (Costa *et al.* 2016). The classical model for a bent-over plume (e.g. Briggs 1984; Weil 1988) assumes $\gamma = \beta'$. An entrainment model which is also valid for weak-crossflow plumes is given by (Devenish *et al.* 2010, DRWT)

$$\gamma = \frac{\sqrt[n]{(\alpha w_m)^n + (\beta' U)^n}}{U_s}. \tag{2.17}$$

The DRWT model uses two parameters, α and β', to account for entrainment due to vertical and horizontal motion, respectively, and assumes that the added-mass coefficient $k = 0$. Here, β' refers to the same bent-over entrainment coefficient as the one that is used in (2.15). A further parameter n determines the function used to combine the entrainment resulting from the vertical and horizontal momentum into a single entrainment quantity. In their paper, Devenish *et al.* (2010) test the values $n = \{1, 1.5, 2\}$ and conclude that $n = 1.5$ provides the best match between the model and their LES data.

3. Numerical modelling

3.1. *Simulation details*

The simulations concern the evolution of a plume in an unstratified environment with a uniform crossflow speed U. A constant integral buoyancy flux F_0 is imposed on a circular area source of diameter $2r_0$, which is positioned at $x = 0$. The source has no initial velocity, which implies the plume is infinitely lazy at the source (Hunt & Kaye 2005). The buoyancy flux is therefore imposed as a diffusive flux using a Neumann boundary condition, which will be transported through a very thin thermal boundary layer before it becomes convectively unstable and starts rising as a conventional plume.

The relevant non-dimensional parameters for buoyant plumes in a crossflow can be formed from the exit velocity $w_0 = M_0^{1/2}/r_0$, the buoyancy velocity scale $U_b = (F_0/r_0)^{1/3}$, the crossflow speed U, and for completeness the viscous and thermal velocity scales ν/r_0 and κ/r_0, respectively. All quantities with subscript zero represent their respective quantities at the source (e.g. M_0 represents M evaluated at the source). From these five velocity scales, four dimensionless quantities can be constructed:

$$R_0 = \frac{w_0}{U}, \quad Ri_0 = \frac{F_0}{r_0 w_0^3} = \frac{b_0 r_0}{w_0^2}, \quad Re_0 = \frac{2F_0^{1/3} r_0^{2/3}}{\nu}, \quad Pr = \frac{\nu}{\kappa}, \tag{3.1a–d}$$

where R_0 is the jet-to-crossflow speed ratio, Ri_0 is the source Richardson number, Re_0 is the source Reynolds number and Pr is the Prandtl number. Note that the Froude number, which is also commonly used, is the square root of the reciprocal of Ri_0. These dimensionless groups are not ideal for the current simulation set-up since $w_0 = 0$ which implies that $w_0/U = 0$ and $Ri_0 = \infty$. In this study, we thus use the crossflow Richardson

Simulation	Ri_U	$N_x \times N_y \times N_z$	$(L_x \times L_y \times L_z)/r_0^3$	β	β'	k	x_v/r_0
S1	8.0	$1152 \times 768 \times 1152$	$24 \times 24 \times 36$	0.68	0.49	0.91	0.45
S2	2.4	$1536 \times 768 \times 960$	$32 \times 24 \times 30$	0.97	0.76	0.62	1.24
S3	1.0	$1728 \times 768 \times 768$	$36 \times 24 \times 24$	1.05	0.83	0.62	1.85
S4	0.5	$1728 \times 576 \times 576$	$36 \times 18 \times 18$	1.15	0.88	0.71	1.91
S5	0.3	$1728 \times 576 \times 576$	$36 \times 18 \times 18$	1.15	0.84	0.86	2.95

Table 1. Simulation details. The source Reynolds number $Re_0 = 1000$ and Prandtl number $Pr = 1$ for all simulations.

number Ri_U, defined as

$$Ri_U = Ri_0 R_0^3 = \frac{F_0}{U^3 r_0} = \frac{U_b^3}{U^3}, \tag{3.2}$$

which is the cube of the ratio of the buoyancy velocity scale U_b to the crossflow speed U. Equivalently, using the buoyancy length scale $\ell_b = F_0/U^3$, Ri_U can be interpreted as a ratio of length scales, $Ri_U = \ell_b/r_0$.

Five simulations S1–S5 have been performed at different values of Ri_U, details of which are presented in table 1. Simulation S1 reproduces a case characterised by a weak crossflow, with $Ri_U = 8$, which corresponds to a flow in which the crossflow speed U is equal to half the buoyancy velocity scale U_b. Simulation S2, with $Ri_U = 2.4$, also represents a weak crossflow. Simulations S4 and S5, with $Ri_U = 0.5$ and $Ri_U = 0.3$, respectively, correspond to strong crossflow cases for which $U > U_b$. Simulation S3 has $Ri_U = 1$, which implies that $U = U_b$. All simulations use an identical source Reynolds number $Re_0 = 1000$ and Prandtl number $Pr = 1$. This value is chosen because it is the highest value at which the simulations may currently be conducted, due to computational cost. This value of Re_0 does ensure that the flow is fully turbulent.

Due to the fact that the strength of the crossflow affects the evolution of the plume, the domain sizes were chosen large enough such that each plume can evolve inside the domain without interacting with its boundaries, but tight enough not to waste computational resources on flow regions where only ambient flow is present. The domain dimensions are given in table 1. Note that the x coordinate ranges from $x/r_0 = -5$ to $x/r_0 = L_x/r_0 - 5$. For all simulations, the percentage of the domain occupied by the plume in the (y, z) plane is less than 9 %. This is sufficient to ensure that the interactions with the boundaries are negligible. For a row of plumes in a quiescent environment, the mean plume boundaries plotted by Rooney (2015) show that a plume which spans ∼25 % of the domain is not significantly affected by the competing entrainment of the other plumes. The grid resolution was chosen such that $\Delta x/\eta_K$ peaks at just below 3 close to the source for all simulations, where $\eta_K = (\nu^3/\varepsilon)^{1/4}$ is the Kolmogorov length scale and $\Delta x = L_x/N_x$ is the grid resolution. The same grid resolution is used in the transverse and vertical directions, so Δx is also equal to L_y/N_y and L_z/N_z. The ratio $\Delta x/\eta_K$ inside the plume decays rapidly as a function of x; it is below 2 within $4r_0$ downstream of the source for all simulations, indicating that the grid resolution is sufficiently high to be considered DNS. Indeed, the peak of the dissipation rate takes place at a scale of $\sim 24\eta_K$ for isotropic turbulence (Pope 2000).

The simulations were performed using the DNS code SPARKLE (Craske & van Reeuwijk 2015), which integrates (2.1) on a cuboidal domain and is fully parallelised using domain decomposition in two directions. The spatial differential operator employs

a fourth-order symmetry-preserving central difference scheme. Incompressibility was enforced by taking the divergence of (2.1) and solving the resulting Poisson equation for p by performing fast Fourier transforms in the lateral directions. A third-order Adams–Bashforth method is used for the time integration.

Periodic boundary conditions were applied in the lateral directions and free-slip boundary conditions were applied at $z = 0$ and $z = L_z$. Zero-flux Neumann boundary conditions were used for buoyancy at $z = 0$ and $z = L_z$, with the exception of a circular region of radius r_0, centred at $(0, 0, 0)$, through which a constant buoyancy flux was imposed. In order to enforce a uniform inflow boundary condition at $x/r_0 = -5$ on our periodic domain we used a nudging region of length L_n at the end of the domain over which the fluid velocity and buoyancy were gradually adjusted to become those of the environment (Stevens, Graham & Meneveau 2014). Denoting the distance from the beginning of the nudging region as x^*, we adjusted the velocity according to $\boldsymbol{u}^* = (1 - x^*/L_n)\boldsymbol{u} + (x^*/L_n)\boldsymbol{u}_a$, where $\boldsymbol{u}$ is the original DNS velocity and $\boldsymbol{u}_a = (U, 0, 0)$ is the ambient environmental velocity. The same linear transition method is used for the temperature. This procedure was implemented immediately prior to applying the pressure correction to maintain incompressibility. For all simulations the nudging length was set to $L_n/r_0 = 4$. Careful analysis of the simulation results was carried out to ensure that the nudging does not affect the statistics upstream, which for an incompressible flow could occur via pressure gradients generated by the nudging. No pressure gradients were observed near the nudging region, implying that it does not contaminate the upstream statistics.

3.2. *Plume identification*

The determination of all integral quantities requires identification of the plume fluid. This was performed by applying a threshold on the average buoyancy $\bar{b}$ with a value of 1 % of the maximum mean buoyancy at fixed x. Examples of the identified plume boundary are shown with a red line in figure 3.

3.3. *Budget calculations*

For the presentation of the budgets (2.6*a–c*) that are discussed in §§ 5 and 6, the entrainment terms E and $\mathcal{L}$ need to be determined. Calculating these directly from the definition in (2.5*a*,*b*) can be challenging, since it requires a boundary integral in the plane perpendicular to the plume, which in turn requires defining the computational cells which constitute the boundary, taking account of any disconnected regions, defining normal vectors and taking into account the fact that the underlying grid is staggered. It is computationally more convenient to use the divergence theorem in reverse to calculate $E[\phi]$ via

$$E[\phi] = -\iint_{\Omega} \frac{\partial \overline{v\phi}}{\partial y} + \frac{\partial \overline{u_\eta \phi}}{\partial \eta}\,\mathrm{d}A \tag{3.3}$$

and to use the original definition of $\mathcal{L}[\phi]$ (van Reeuwijk *et al.* 2021):

$$\mathcal{L}[\phi] = \frac{\mathrm{d}}{\mathrm{d}s}\iint_{\Omega} \overline{u_s\phi}\,\mathrm{d}A - \iint_{\Omega} \frac{\partial \overline{u_s\phi}}{\partial s}\,\mathrm{d}A. \tag{3.4}$$

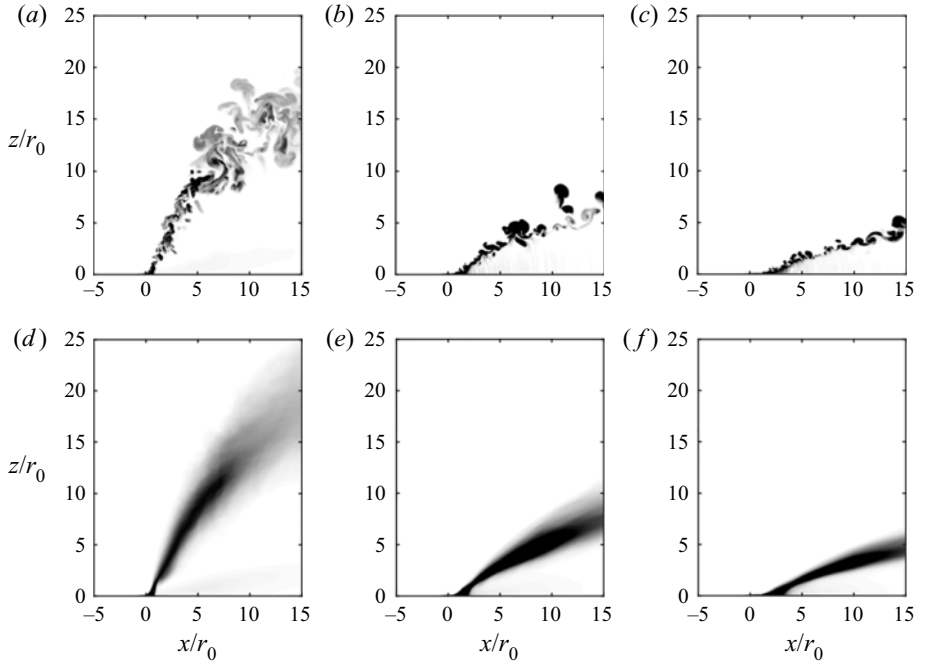

Figure 2. Cross-section at the $y = 0$ centre plane of the instantaneous (*a–c*) and time-averaged (*d–f*) buoyancy field. (*a*,*d*) Simulation S1. (*b*,*e*) Simulation S3. (*c*,*f*) Simulation S5.

4. Plume evolution and geometry

4.1. *General plume behaviour*

Instantaneous and time-averaged snapshots of the buoyancy field b in the (x, z) plane are shown in figure 2, normalised by $b_{max}(x) = \max_{y,z} \bar{b}$. The plume, which is infinitely lazy at the source, must first diffuse through the thermal boundary layer at the wall, during which time it is advected downstream by the crossflow. Once the plume has traversed the thermal boundary layer (which typically occurs between 0.5 and 2 source radii downstream depending on the crossflow speed), the plume accelerates upwards, causing some necking in the y direction. Following this, the plume angle φ gradually decreases as the plume rises through the ambient, and the plume radius increases due to turbulent entrainment. This increase is clearly dependent on the flow speed: the plumes are observed to be narrower for higher crossflow speeds. Another notable feature of these snapshots is that there is a tendency for a small amount of buoyancy to be swept into the wake of the plume. The buoyancy detrains from the plume close to the source as a result of the initial transition instabilities, and remains close to the $z = 0$ boundary. This requires some careful attention when it comes to determining the plume boundary because in general it is inappropriate to regard this region, which may have a small amount of buoyancy but is otherwise quiescent, as being within the plume. For clarity we have removed the buoyancy concentration that would be in these quiescent regions from the figure. Cross-sections in the (y, η) plane at $s/r_0 = 5$ are shown in figure 3. These clearly show a buoyant core structure with twin vortices, which becomes narrower and less diffuse as the crossflow speed increases.

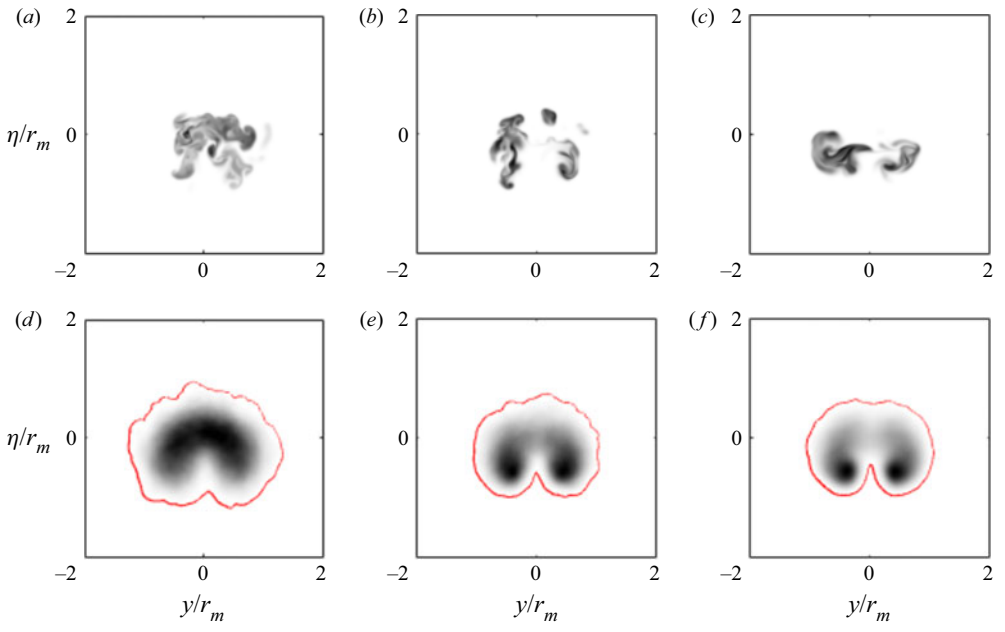

Figure 3. The buoyancy field in the (y, η) plane at $s/r_0 = 5$, for the (*a–c*) instantaneous buoyancy and (*d–f*) time-averaged buoyancy. (*a*,*d*) Simulation S1. (*b*,*e*) Simulation S3. (*c*,*f*) Simulation S5. The red line in (*d–f*) is the applied threshold on buoyancy at 1 % of the maximum of the time-averaged value.

4.2. *Plume centreline*

The plume centreline is a fundamental quantity in integral plume models. Theoretically, it is typically represented as the central streamline of the plume (e.g. Weil 1988). This is relatively straightforward to do using numerical simulation when the full velocity field is known (Yuan & Street 1998; Yuan *et al.* 1999; Muppidi & Mahesh 2005; De Wit *et al.* 2014; Cintolesi *et al.* 2019) via a streamline that starts at the centre of the source. Most laboratory studies, but also some numerical studies (Devenish *et al.* 2010), use either the maximum velocity or buoyancy or use the centre of mass of the buoyancy/passive scalar or velocity (Contini *et al.* 2011).

Shown in figure 4 are a number of centreline definitions as a function of x, plotted together with isolines of the buoyancy averaged over the plume width (in y) for simulation S3. The centre of mass was calculated according to

$$z_c(x) = \frac{\iint_\Omega z\bar{b}\,\mathrm{d}y\,\mathrm{d}z}{\iint_\Omega \bar{b}\,\mathrm{d}y\,\mathrm{d}z}. \tag{4.1}$$

Here, integration is performed over the plume fluid area Ω. Extracting the central streamline z_U required some careful consideration as the plume is infinitely lazy at its source, implying that the velocities are zero on the boundary. This makes it impossible to start a streamline in the centre of the source. Instead, we let the streamline start at $z_c(x = 2r_0)$, which is where the plume lifts off from the surface. As can be seen, all the other plume trajectory indicators are practically identical at that stage. The maximum buoyancy, velocity and turbulent kinetic energy were determined by taking the mean value across the plume width (in the y direction), and then finding the maximum value for

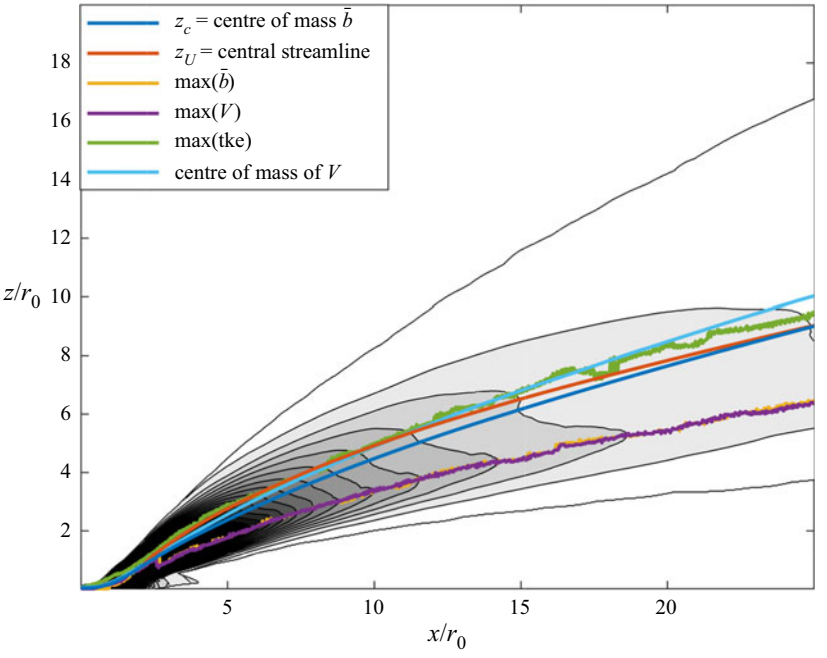

Figure 4. Various estimates for the plume centreline, based on simulation S3 (tke, turbulent kinetic energy). The isocontours denote the average buoyancy across the plume width.

each x. By averaging over the plume width, the centreline represents the entire plume area. Finally, a trajectory is shown that is based on the centre of mass of the velocity $V = \sqrt{\bar{u}^2 + \bar{w}^2}$, using (4.1) but substituting $\bar{b}$ with V.

Near $x = 0$, some discontinuities can be seen in the buoyancy isocontours which are associated with the plume lift-off from the ground and that will not be considered in the analysis in the remainder of the paper. The central streamline z_U and centre of mass z_c evolve very similarly, although z_U has a slightly higher trajectory initially and then follows a slightly smaller slope further downwind. The maxima of the buoyancy and velocity are very similar, and follow a trajectory which is lower than the centres of mass and the maximum turbulent kinetic energy. Figure 2 suggests that the maximum of buoyancy will roughly align with the vortex centres of the double-roll structures, where buoyancy accumulates. Unsurprisingly, the centres of mass change much more smoothly than the centrelines based on finding a maximum. The centre of mass trajectory based on V is slightly higher than that of $\bar{b}$, but this is a small difference compared with the difference between z_c and z_U.

4.3. *Plume angle*

Having calculated the integral plume quantities, we verify whether the plume slope φ is identical to the mean velocity streamline angle φ_u (2.13), which would imply that

$$\frac{\mathrm{d}z_c}{\mathrm{d}x} = \frac{w_m}{U + u_m} = \frac{M_z}{QU + M_x}. \tag{4.2}$$

This relation is plotted in figure 5 for simulation S3, together with the gradient of z_c and z_U. Figure 5 shows that $w_m/(U + u_m) = M_z/(QU + M_x)$ is nearly half of $\mathrm{d}z_c/\mathrm{d}x$ and $\mathrm{d}z_U/\mathrm{d}x$, and therefore implies that the ratio of the integral momentum fluxes is a poor estimate

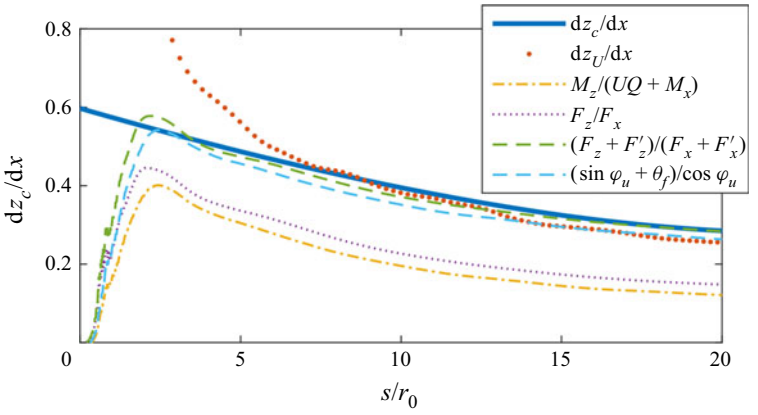

Figure 5. Slope of the plume centreline for simulation S3, together with several integral-quantity estimates.

of the plume slope. Note that z_c was approximated by two cubic splines in order to avoid numerical errors resulting from repeated differentiation (see Jordan (2021) for details). Simulation S3 is representative of the other simulations. Figure 5 shows that the streamline angle $w_m/(U + u_m)$ is not identical to the plume angle for z_c or z_U. The assumption that the plume centre of mass follows a streamline dictated by w_m and $U + u_m$ is central to the integral theory of plumes in a crossflow. Therefore, the implications of the observed discrepancy are substantial.

Figure 6(a) shows the velocity streamlines through the plume for simulation S3. The streamlines were constructed from the velocity inside the plume, by integrating the velocity over the y direction within the plume and then dividing through by the local plume width, thereby obtaining a velocity field representative across the width of the plume. Figure 6(a) is consistent with figure 5 in demonstrating that the angle of the streamlines is substantially different from the plume centreline (thick black line), for both z_c and z_U. The reason that z_U is not aligned with the mean streamlines across the plume is the double-roll structure which causes positive vertical velocities on the centreplane and negative velocities away from the centreplane. For the case under consideration (S3), the streamlines enter the top of the plume (indicated by a dashed line) at nearly 45°, but have much smaller angles near the bottom boundary. However, neither the centre of mass of the plume z_c (thick black line) nor the central streamline z_U (thick dashed black line) is parallel to the streamlines. Thus, the plume angle φ is different from the velocity angle φ_u, which implies that the conventional assumption of the plume aligning with the central velocity streamline ($\varphi = \varphi_u$) is violated.

Since z_c was determined from the centre of mass of the buoyancy of the plume, it stands to reason to investigate whether it is more suitable to consider field lines based on the local mean buoyancy flux $\bar{\boldsymbol{f}} = (\bar{u}\bar{b}, \bar{w}\bar{b})$, which are shown in figure 6(b). Similar to the mean velocity, the mean buoyancy flux was determined by integrating the individual components over y and dividing by the local plume width. Although the mean buoyancy field lines follow the bottom boundary almost perfectly, it is clear that the behaviour is nearly identical to that of figure 6(a).

It is only when turning to the field lines of the total buoyancy flux $\boldsymbol{f} = (\bar{u}\bar{b} + \overline{u'b'}, \bar{w}\bar{b} + \overline{w'b'})$ that the field lines are found to be fully representative of z_c. The central streamline z_U also correlates well with these field lines, even when z_U is based on the velocity field only. A secondary conclusion that can be drawn from comparing figures 6(b) and 6(c) is that the

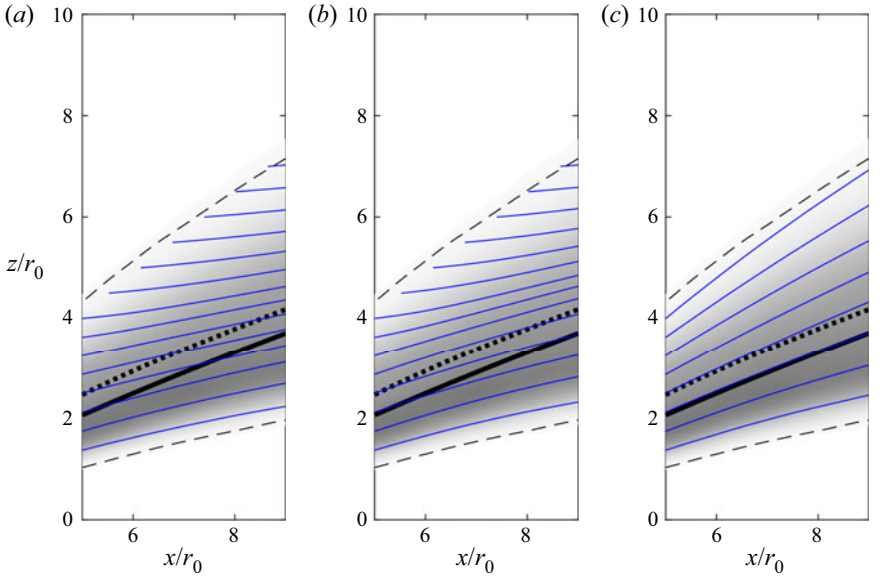

Figure 6. Streamlines (blue) for simulation S3, together with z_c (thick black line), z_U (thick dotted line), the plume boundaries (dashed line) and the y-averaged buoyancy field (in grey). Streamline quantities are averaged in y across the local plume width. (*a*) Streamlines of $\boldsymbol{u} = (\bar{u}, \bar{w})$. (*b*) Field lines of $\bar{\boldsymbol{f}} = (\bar{u}\bar{b}, \bar{w}\bar{b})$. (*c*) Field lines of $\boldsymbol{f} = (\bar{u}\bar{b} + \overline{u'b'}, \bar{w}\bar{b} + \overline{w'b'})$.

region below the plume centreline is dominated by mean buoyancy transport and the top by a combination of mean and turbulent buoyancy fluxes. This is consistent with previous observations (Huq & Stewart 1997). Furthermore this image suggests that the plume is entraining strongly at the top. It is likely that the high degree of turbulence towards the top of the plume and the impinging crossflow contribute to the strong entrainment there. The fact that the total buoyancy transport determines the angle of the plume is verified in figure 5, which is shown to follow $\mathrm{d}z_c/\mathrm{d}x$ very closely.

Similar conclusions can be drawn from the integral fluxes by defining decomposed fluxes for F and F':

$$F_x = \frac{1}{\pi}\iint_{\Omega} \bar{u}\bar{b}\,\mathrm{d}A, \quad F_z = \frac{1}{\pi}\iint_{\Omega} \bar{w}\bar{b}\,\mathrm{d}A, \tag{4.3a,b}$$

$$F'_x = \frac{1}{\pi}\iint_{\Omega} \overline{u'b'}\,\mathrm{d}A, \quad F'_z = \frac{1}{\pi}\iint_{\Omega} \overline{w'b'}\,\mathrm{d}A. \tag{4.4a,b}$$

Shown in figure 5 is F_z/F_x, which is the approximation of $\mathrm{d}z_c/\mathrm{d}x$ based on mean buoyancy fluxes in the horizontal and vertical directions. It is clear that this result is very similar to that given by the $w_m/(U + u_m)$ estimate for $\mathrm{d}z_c/\mathrm{d}x$, consistent with figure 6(*a*,*b*). Defining the slope based on the total buoyancy flux as $\mathrm{d}z_c/\mathrm{d}x = (F_z + F'_z)/(F_x + F'_x)$, consistent with figure 6(*c*), produces an accurate estimate of the plume slope $\mathrm{d}z_c/\mathrm{d}x$. For this reason, z_c is used to represent the plume trajectory from this point onwards. From the observation that $M_z/(UQ + M_x) \approx F_z/F_x$ (figure 5), the plume angle can be approximated as follows:

$$\frac{\mathrm{d}z_c}{\mathrm{d}x} \approx \frac{F_z + F'_z}{F_x + F'_x} \approx \tan\varphi_u + \frac{F'_z}{F_x} = \frac{\sin\varphi_u + \theta_f}{\cos\varphi_u}, \tag{4.5}$$

where $\theta_f = F'_z/F$. In arriving at the result above, use was made of (2.13), $F'_x \ll F_x$ (justified from analysing the DNS data) and using that $F_x/F \approx \cos\varphi_u$ since

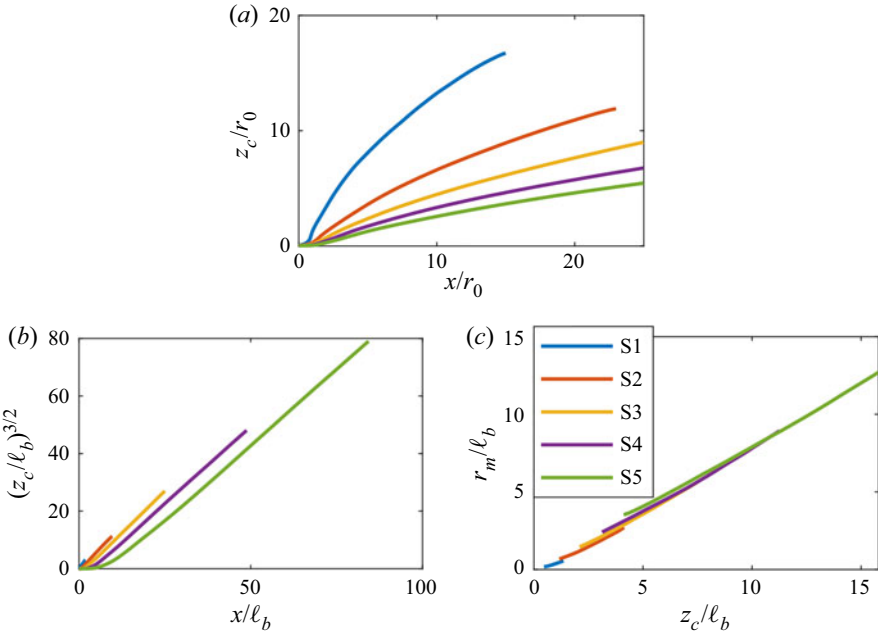

Figure 7. Plume trajectories. (*a*) Centreline z_c as a function of x. (*b*) $z_c^{3/2}$ as a function of x. (*c*) Plume radius r_m as a function of z_c.

$F = \sqrt{F_x^2 + F_z^2}$. The ratio of the turbulent buoyancy flux to the mean buoyancy flux F_z'/F was denoted θ_f in van Reeuwijk & Craske (2015), which motivates its name in the current paper. An *a priori* calculation of $\mathrm{d}z_c/\mathrm{d}x$ using (4.5) is shown in figure 5 which shows good agreement with the observed plume angle. The comparison of $\mathrm{d}z_c/\mathrm{d}x$ with parameterised θ_f for all cases is shown in § 5.

4.4. *Integral fluxes*

The plume centrelines z_c are shown as a function of x/r_0 in figure 7(*a*) for all simulations. In order to validate the simulations, we compare these centrelines with the analytical prediction (2.16) of a bent-over plume. Shown in figure 7(*b*) is $(z_c/\ell_b)^{3/2}$ against x. As can be observed, all plume trajectories evolve in a linear fashion, confirming scaling consistent with the expected bent-over plume behaviour. The advantage of plotting $(z_c/\ell_b)^{3/2}$ against x in a linear plot, rather than (z_c/ℓ_b) against x in a log–log plot, is that the power-law exponent extracted from a log–log plot can be strongly influenced by the virtual origin correction. Comparison with experimental and numerical data of plumes in crossflow is carried out based on the fit to (2.16), rather than displaying them in figure 7 (as the main difference would be the slope, which depends on R_0; Briggs 1984).

By fitting a straight line through the last part of the trajectory for each simulation shown in figure 7(*b*), β' and the virtual origin x_v can be identified. Figure 7(*c*) shows the linear dependence between r_m and z_c, conforming with the bent-over plume predictions (2.15). The values of β, β', k and x_v/r_0 are presented in table 1 for each simulation. They are calculated from (2.15) and (2.16) and from the observations in figure 7.

We find values of β' in the range $0.49 \leq \beta' \leq 0.88$ which is higher than in the experiments of De Wit *et al.* (2014), and the LES of Cintolesi *et al.* (2019), suggesting

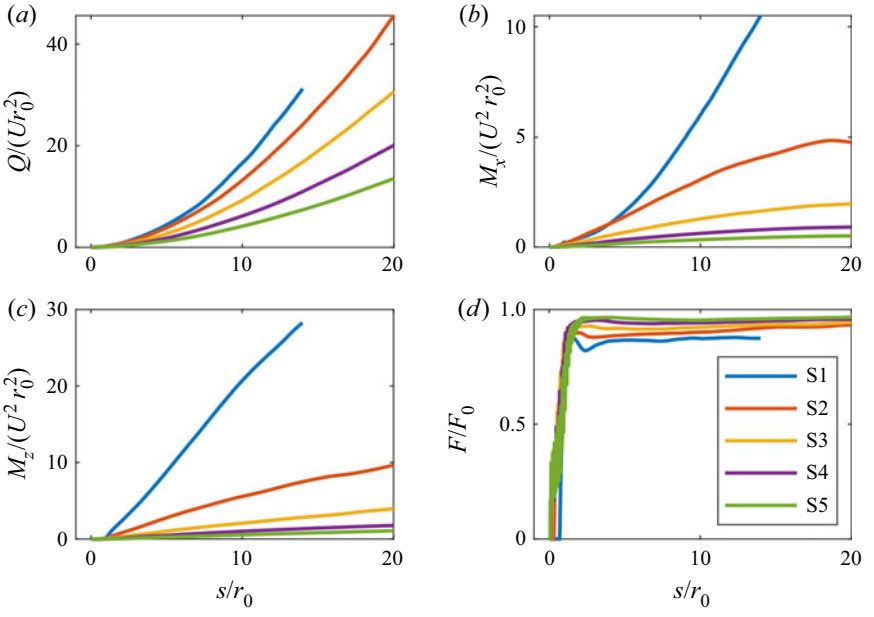

Figure 8. Integral plume quantities as a function of s for each simulation. (a) Volume flux Q. (b) Horizontal momentum excess flux M_x. (c) Vertical momentum flux M_z. (d) Buoyancy flux F.

the plumes considered here ascend less rapidly. We suspect these higher values of β' are due to the fact that the plume under consideration is infinitely lazy at the source. Indeed, Briggs (1984) developed an empirical prediction $\beta' = 0.4 + 1.2/R_0$ for the dependence of β' on $R_0 = w_0/U$, demonstrating that this parameter depends on conditions at the source, particularly at low values of R_0.

Once the plume trajectory and the plume fluid have been identified, the integral volume flux Q, horizontal momentum excess flux M_x and vertical momentum flux M_z can be calculated from their definitions (2.9a–d). These quantities are shown in figure 8 as a function of s. The volume flux Q grows increasingly fast as it evolves due to the plume's increasing size (see § 5). Contrary to the conventional assumptions, the horizontal momentum excess flux M_x is not conserved for the plumes. Instead, it increases with s. This is caused by the pressure gradient term P_x in (2.6b), which is non-zero. Simulation S1 is clearly of a different character from the other simulations, as the second derivative of M_x is of opposite sign. The vertical momentum flux M_z also grows as a function of s. Unlike M_x, this quantity is expected to be non-zero due to the influence of buoyancy in (2.6c). However, the influence of pressure is non-negligible for this quantity also. Consistent with figure 8(a,b), the larger the crossflow speed U, the smaller the gradient, but this can be partially explained by the way in which the figures are normalised. The physical interpretation of these effects on the momentum fluxes is that the pressure field, which is generated by the interaction of the crossflow with the leading edge of the plume, transfers some of the upward momentum generated by the buoyancy into horizontal momentum. This leads to M_x being higher than expected, while M_z is lower than expected. The role of pressure is investigated in further detail in § 6.

The mean buoyancy flux F increases rapidly as measured from the centre of the source as it is advected by the mean flow, and the initially diffusive buoyancy flux is transferred to an advective flux, which is displayed here. The buoyancy flux is practically constant

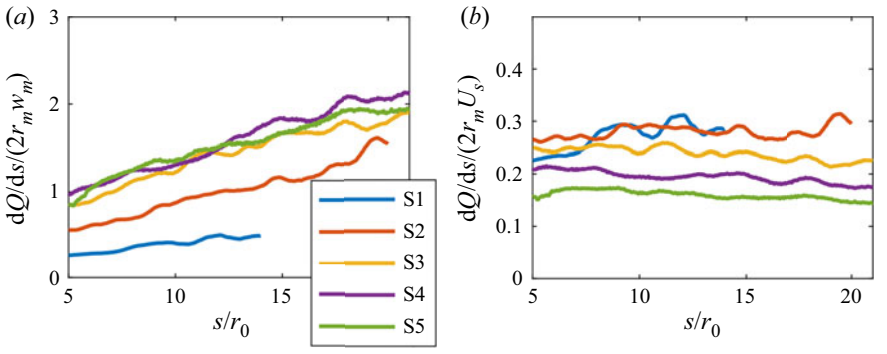

Figure 9. Entrainment coefficients based on different parameterisations. (*a*) Coefficient $\gamma = \mathrm{d}Q/\mathrm{d}s/(2r_m w_m)$. (*b*) Coefficient $\gamma_U = \mathrm{d}Q/\mathrm{d}s/(2r_m U_s)$.

across all simulations within two source diameters of the source, and remains close to its initial value F_0. This is consistent with the buoyancy flux equation (2.11*d*). The value of the mean buoyancy flux F_0 differs from unity because a part of the buoyancy transport is due to turbulence. Turbulence transports a higher percentage of the buoyancy for weaker crossflows, reaching a limiting value of approximately 20 % in the absence of wind (van Reeuwijk *et al.* 2016).

5. Entrainment parameterisation

The DNS data enable direct evaluation of the relationship between the entrainment flux and characteristic plume radius and vertical velocity (2.10). If (2.10) holds, implying that r_m and w_m are the appropriate length and velocity scales to be used to parameterise the entrainment coefficient, then the entrainment coefficient $\gamma \equiv \mathrm{d}Q/\mathrm{d}s/(2r_m w_m)$ will be constant and the same for all simulations. Figure 9(*a*), where we plot γ as a function of s/r_0, shows that this is not the case. Indeed, γ is an increasing function of s for all simulations and the slope of $\gamma(s)$ does not suggest an asymptote to a limiting value. It appears though that S3–S5 converge to an identical value. The fact that γ is not constant in figure 9(*a*) indicates that the parameterisation (2.10) is inadequate to describe the data from these simulations. Given that r_m represents the plume circumference over which entrainment takes place in (2.10), there are no obvious other candidate length scales for this quantity. This suggests that w_m might not be the appropriate velocity scale for parameterising the entrainment in these cases.

Another choice of the characteristic plume velocity is to use U_s, which implies an entrainment closure given by

$$E + \mathcal{L} = 2\gamma_U r_m U_s, \tag{5.1}$$

where γ_U is the entrainment coefficient based on U_s. From figure 9, it can be seen that γ_U is approximately constant as a function of s, although the value of γ_U decreases with increasing crossflow speed U. The ansatz (5.1), therefore, can serve as the basis for a parameterisation.

Shown in figure 10 is the integral budget for the continuity equation (2.6*a*) for simulations S1, S3 and S5, which provides insight into the two identified modes of entrainment: flow of fluid into the plume (E) and incorporation of ambient fluid due to expansion of the plume ($\mathcal{L}$). As U increases (Ri_U decreases), $\mathcal{L}$ becomes increasingly dominant. Physically, this implies that for sufficiently large U, the main contribution to the

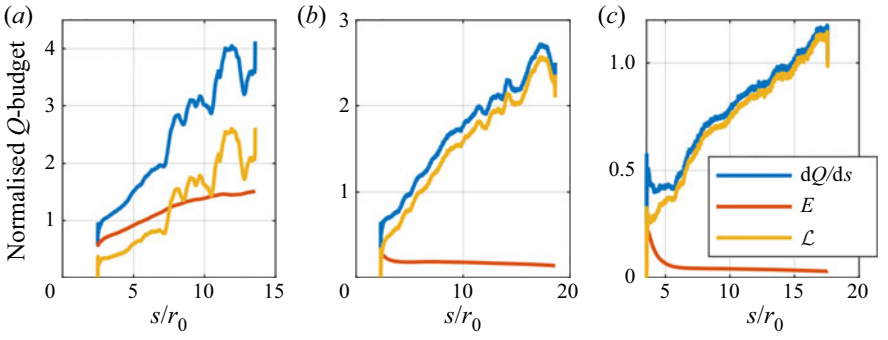

Figure 10. Budget of the integral continuity equation, normalised by Ur_0. (*a*) Simulation S1. (*b*) Simulation S3. (*c*) Simulation S5.

volume flux is not flow directly into or perpendicular to the plume, but rather incorporation as the plume expands of new ambient fluid with non-zero velocity. On this basis we may assume that the Leibniz term is the dominant contribution to the volume flux, implying that $\mathrm{d}Q$ equals $\mathcal{L}\,\mathrm{d}s$. As the local plume angle is φ, the height increment of the plume is $\mathrm{d}z = \sin\varphi\,\mathrm{d}s$. Assuming that the plume width is $2ar_m$, where a is an empirical constant, the volume flux increment $\mathcal{L}\,\mathrm{d}s = 2aUr_m\,\mathrm{d}z = 2Uar_m\sin\varphi\,\mathrm{d}s$, and thus

$$\mathcal{L} = 2aUr_m\sin\varphi. \tag{5.2}$$

Upon equating this expression for $\mathcal{L}$ with the entrainment ansatz (5.1), we obtain

$$\gamma_U = a\frac{U}{U_s}\sin\varphi = a\frac{U}{U_s}\frac{\mathrm{d}z_c}{\mathrm{d}s}. \tag{5.3}$$

Shown in figure 11(*a*) is the correlation between $\mathrm{d}Q/\mathrm{d}s$ and $\mathcal{L} = 2aUr_m\sin\varphi$. The data bound the value of a between 0.5 and 1. We use the value $a = 0.9$ here, which approximates simulations S3–S5 in particular. Parameterisation of γ_U will require $\mathrm{d}z_c/\mathrm{d}s$ which is defined via (4.5). In this expression the only term that requires parameterisation is θ_f, since the velocity components will be known as part of the integral plume model. In general, we expect that F_z' will depend on the initial conditions Ri_U and the relative vertical velocity $R = w_m/U$.

The value of θ_f is shown as a function of Ri_U in figure 11(*b*). Here, the value of θ_f was averaged over the entire range of s shown in figure 9. The circles denote the average value, and the spread in θ_f over s is shown by the vertical lines. As can be seen, this variation is relatively small, indicating that θ_f is approximately constant for the range of s considered in this paper. The data can be approximated by the following empirical fit:

$$\theta_f = \theta_{fb} + (\theta_{fp} - \theta_{fb})\left(1 - \exp\left[-\left(\frac{Ri_U}{Ri_{U0}}\right)\right]\right), \tag{5.4}$$

which for $Ri_U \to \infty$ represents the pure plume case, for which $\theta_{fp} = 0.20$, and $Ri_U \to 0$ represents the bent-over limit for which $\theta_{fb} = 0.06$. The parameter Ri_{U0} is a constant which determines the cross-over value for the two regimes, and has the value $Ri_{U0} = 1.2$.

It should be noted that for the cases under consideration, θ_f is predominantly determined by the initial condition Ri_U and not R. It would stand to reason that at some point downstream of the source, the plume 'forgets' about its origins and θ_f scales with R, but this is not observed in the limited downstream range simulated here. Further work

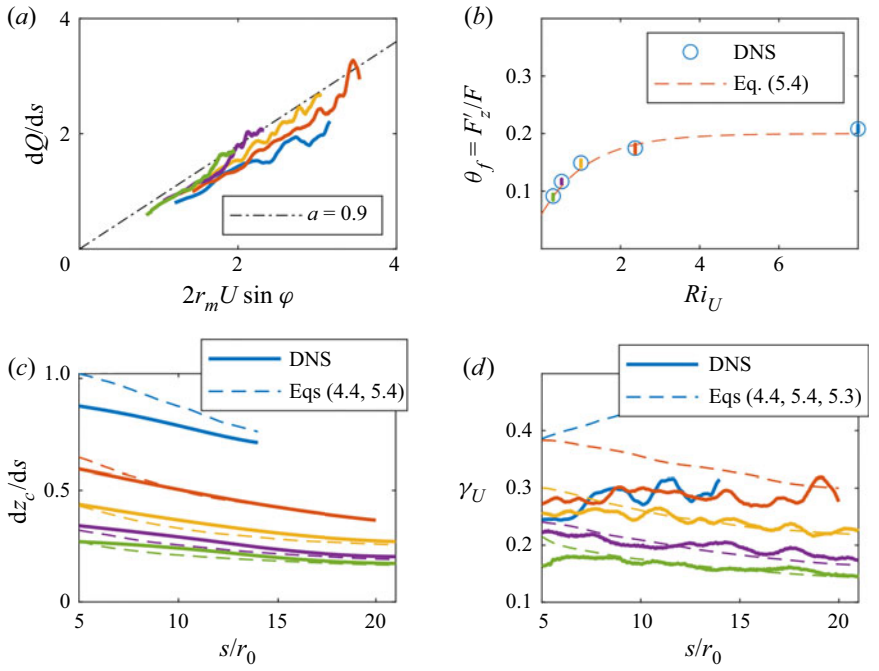

Figure 11. Entrainment parameterisation. (*a*) Plot of $\mathrm{d}Q/\mathrm{d}s$ against $2r_mU\sin\varphi$. A linear relationship indicates a constant γ_U coefficient. (*b*) Entrainment flux; θ_f as a function of Ri_U. (*c*) Slope $\mathrm{d}z_c/\mathrm{d}s$. (*d*) Coefficeient γ_U. Colour scheme consistent with figure 8. The DNS data and the parameterisation are shown in solid and dashed lines, respectively.

is needed to provide a more complete model of θ_f. An estimate of the range of validity for the current model is made in § 8.

Figure 11(*c*) shows the actual (solid line) and predicted (dashed line) plume-centreline slope $\mathrm{d}z_c/\mathrm{d}x$ for all five simulations based on parameterisations (4.5) and (5.4). As can be seen, the parameterisation predicts the slopes reasonably well, with the exception of the slope for S1, which is slightly underpredicted. Finally, the prediction for γ_U is shown in figure 11(*d*). The entrainment coefficient γ_U, based on parameterisations (4.5), (5.3) and (5.4), is predicted well for simulations S3–S5 but is overpredicted for the weaker crossflow simulations S1 and S2. This is due to the fact that the entrainment model was formulated using the assumption that the Leibniz term $\mathcal{L}$ dominates over the radial entrainment term E. This assumption is only valid for plumes in a strong crossflow with $Ri_U \ll 1$, so the overprediction of γ_U at low crossflow speeds is to be expected. The reliance on the assumption that E is small relative to $\mathcal{L}$ is also likely to be the reason that the slope for S1 is slightly underpredicted.

6. The role of pressure

In this section, we explore the behaviour of the momentum balances (2.6*b*) and (2.6*c*). Figure 12 shows the momentum budget in the x direction (figure 12*a–c*) and the z direction (figure 12*d–f*) for simulations S1, S3 and S5. The entrainment and Leibniz terms have been combined, since it has been established that $\mathcal{L}$ is the dominant term for bent-over plumes. Figure 12(*a–c*) shows clearly that M_x is influenced by the integral pressure gradient P_x, and that the entrainment and Leibniz terms also contribute to M_x, albeit to a lesser extent,

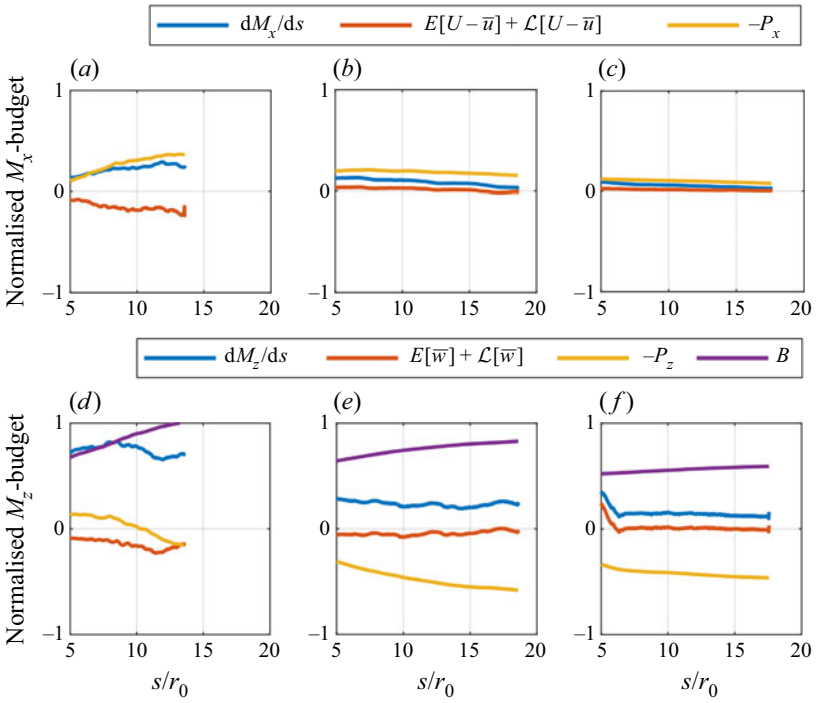

Figure 12. Budgets for the integral momentum equations in the x direction (*a–c*) and z direction (*d–f*), normalised by U^2/r_0. (*a*,*d*) Simulation S1. (*b*,*e*) Simulation S3. (*c*,*f*) Simulation S5.

which represents additional streamwise momentum being incorporated from outside the plume.

The budget of the integral vertical momentum flux is primarily influenced by the buoyancy and integral pressure gradient terms. The buoyancy generates vertical momentum, whereas the integral pressure gradient acts to suppress vertical momentum, counteracting a large portion of the work done by the buoyancy. Integral models that do not take into account this term (either directly or via an added-mass contribution) can therefore be expected to overestimate the vertical velocity inside the plume. The Leibniz terms for incorporation of vertical momentum are negligible.

In order to gain further understanding into what underlies the observed behaviour of P_x and P_z, we display the pressure in the (y,η) plane $s/r_0 = 3$ in figure 13, together with the velocity vectors. Here, the crossflow contribution $U\sin\varphi$ has been subtracted from the velocity vectors to emphasise the net circulation inside the plume (it would otherwise be dominated by $U\sin\varphi$). The adjusted velocity vectors display the anticipated double-roll geometry of a turbulent plume in a crossflow. Note that the crossflow contribution has been subtracted, and thus that the majority of the entrainment occurs at the top of the plume rather than at the bottom of the plume as the figure may seem to suggest.

On the plume top, a high-pressure region is observed whilst there is a low-pressure region on the bottom. Because the plume cross-section is in the (y,η) plane, which is at an angle φ with the horizontal, a difference in pressure values between the top and bottom of the plume indicates a pressure gradient in both the vertical and streamwise directions. This pressure arrangement causes the horizontal integral pressure gradient $-P_x$ to be positive and thus acts to accelerate the plume, whilst it causes $-P_z$ to be negative

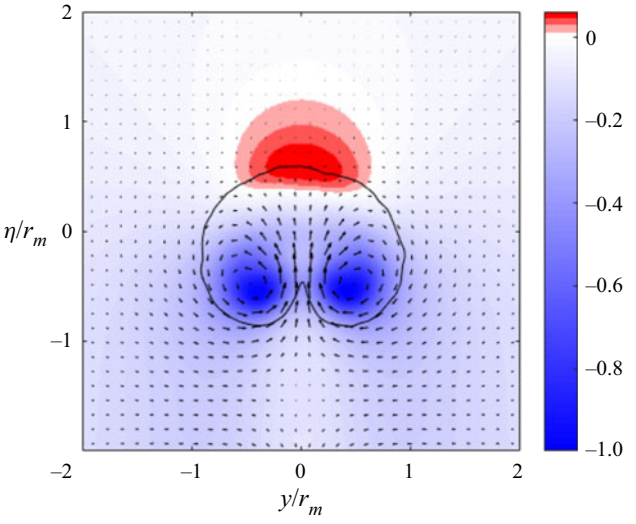

Figure 13. Pressure in a plane perpendicular to the plume at $s/r_0 = 3$ for simulation S3. The pressure has been normalised by its maximum value, and the solid line denotes the plume boundary. The velocity vectors are the (u_y, u_η) components, where the crossflow component has been subtracted to emphasise the flow relative to the background flow.

and thus acts to oppose the buoyancy forcing. Large negative pressures can be observed in the core of the two vortices. The pressure field also demonstrates that the origin of the double-roll structure of plumes in crossflows is the high-pressure area on the topside of the plume. This is consistent with earlier explanations that the double-roll structure is due to the interaction between the crossflow and the leading edge of the plume (Yuan *et al.* 1999; Frolich, Denev & Bockhorn 2004), since the crossflow causes an increase of pressure on the plume's upstream side as the ambient flow needs to be deflected around it. This high-pressure region then in turn creates a double-roll structure inside the plume. A pressure-based explanation of the double-roll structure using a two-dimensional model was also provided in Muppidi & Mahesh (2006). Indeed, the upflow in the centre of the plume will be halted by the presence of an adverse pressure gradient near the top of the plume, and will be deflected sideways, causing the double-roll structure.

The observations above make clear that a model is required for the pressure terms P_x and P_z. Here, the momentum equation in the η direction is a convenient starting point, since this balance can be expected to be dominated by buoyancy and pressure. The integral momentum flux in the η direction is given by $M_\eta = M_z \cos\varphi - (QU + M_x)\sin\varphi$. Differentiating this expression with respect to s results in

$$\frac{\mathrm{d}M_\eta}{\mathrm{d}s} = \frac{\mathrm{d}M_z}{\mathrm{d}s}\cos\varphi - \left(\frac{\mathrm{d}Q}{\mathrm{d}s}U + \frac{\mathrm{d}M_x}{\mathrm{d}s}\right)\sin\varphi - M_s\frac{\mathrm{d}\varphi}{\mathrm{d}s}, \tag{6.1}$$

where $M_s = M_z \sin\varphi + (QU + M_x)\cos\varphi$ is the streamwise momentum flux. Now, substituting (2.6*a*)–(2.6*d*) and using that $E \ll \mathcal{L}$ (valid for strong crossflows) results in

$$\frac{\mathrm{d}M_\eta}{\mathrm{d}s} = -P_\eta + B\cos\varphi - \mathcal{L}U\sin\varphi - M_s\frac{\mathrm{d}\varphi}{\mathrm{d}s}, \tag{6.2}$$

where $P_\eta = P_z\cos\varphi - P_x\sin\varphi$ is the integral pressure gradient in the η direction. In the equation above, the entrainment contributions E and $\mathcal{L}$ in the momentum equations

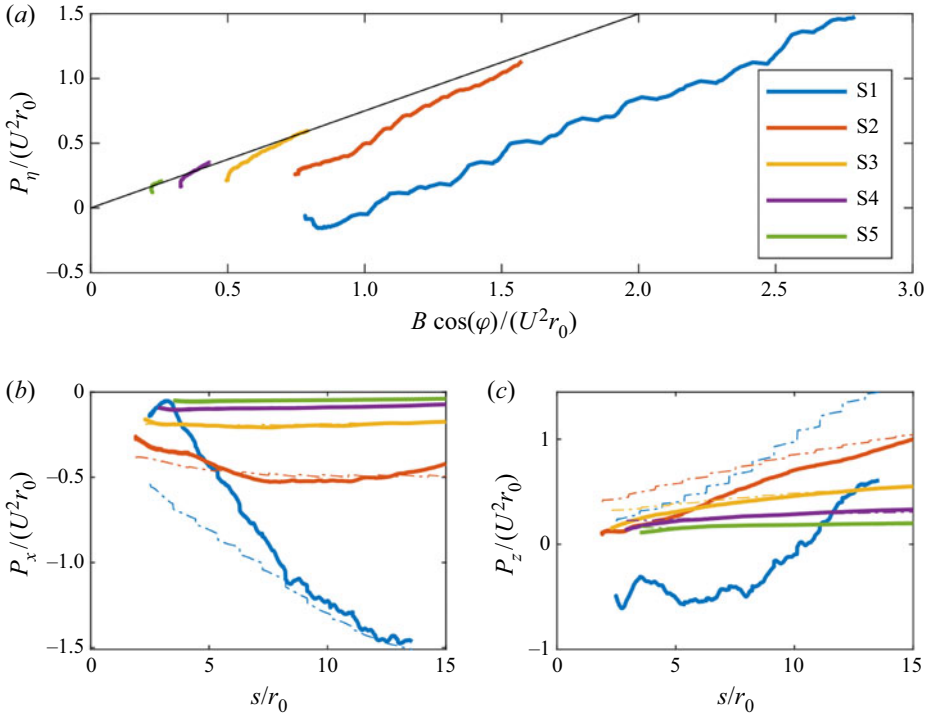

Figure 14. Pressure parameterisation. (*a*) The relation between P_η and B. The solid line is the relation $P_\eta = cB\cos\varphi$, with $c = 0.8$. (*b*) Comparison of simulations (solid lines) and model predictions (dash-dotted lines) for P_x (6.4*a*). (*c*) Comparison of simulations and model predictions for P_z (6.4*b*).

were neglected, consistent with the observations in figure 12 which showed that these are small relative to the other terms in the balance. For the x-momentum equation, this is justified by assuming that $u_m \ll U$. Consistent with conventional plume theory (Morton *et al.* 1956), the integrals of the turbulent momentum fluxes were neglected, since they are much smaller than the integrals of their respective mean momentum fluxes.

We expect that the main balance of forces in the η direction is between pressure and buoyancy and will assume that all the other terms act in proportion to the buoyancy, suggesting a model as follows:

$$P_\eta \sim B\cos\varphi. \tag{6.3}$$

The relation between P_η and $B\cos\varphi$ is plotted in figure 14(*a*), and shows that these variables are proportional as expected. The stronger crossflow simulations S3–S5 converge onto a line. The weaker crossflow simulations have the same slope but are offset. The parameterisation $P_\eta = cB\cos\varphi$ with $c = 0.8$ fits simulations S3–S5 reasonably well. For the lower flow speeds (higher Ri_U), a more sophisticated model is needed. Upon assuming that the integral streamwise pressure gradient P_s is negligible compared to P_η, P_x and P_z are given by

$$P_x = -P_\eta\sin\varphi = -cB\cos\varphi\sin\varphi, \tag{6.4a}$$

$$P_z = P_\eta\cos\varphi = cB\cos^2\varphi. \tag{6.4b}$$

These relations are plotted in figure 14(*b*,*c*) for all simulations (dash-dotted lines) and it can be seen that they capture the pressure contributions well, particularly those for S3–S5, where it is hard to distinguish between the simulation data and the model prediction.

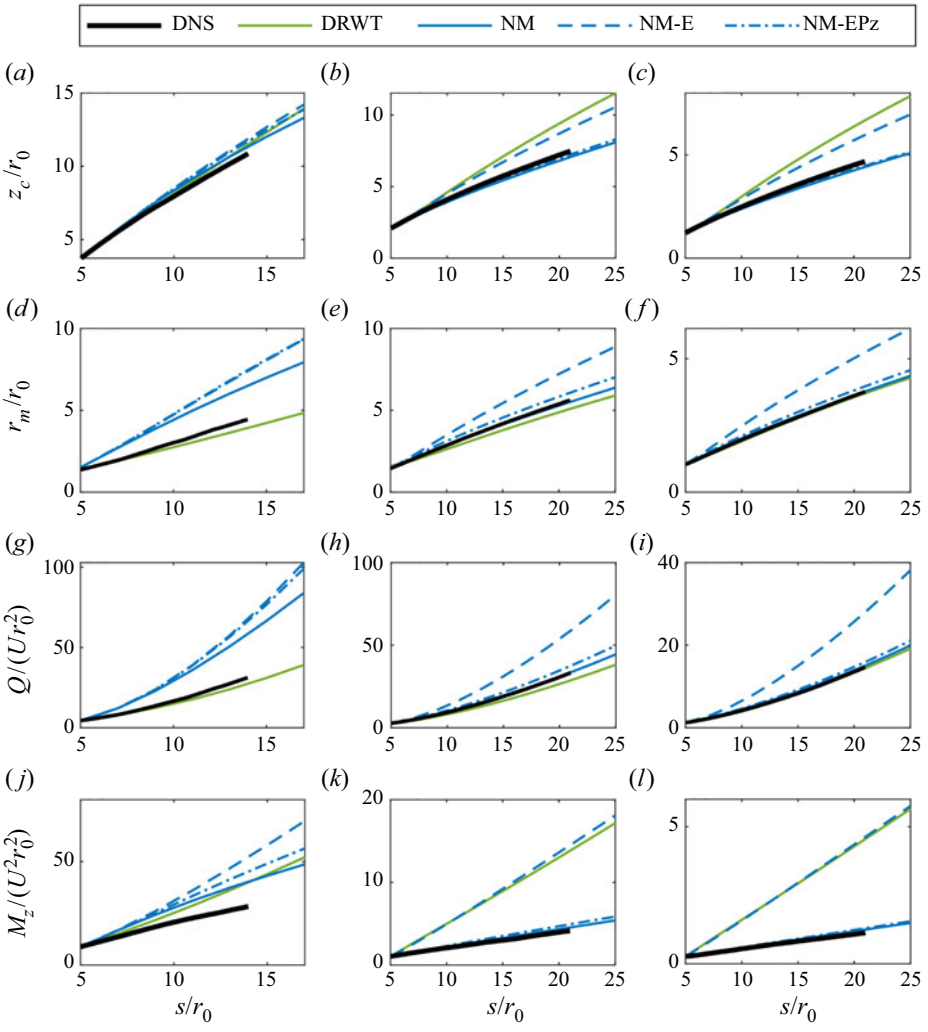

Figure 15. Comparison of DNS data for simulations S1 (*a*,*d*,*g*,*j*), S3 (*b*,*e*,*h*,*k*) and S5 (*c*,*f*,*i*,*l*) with the DRWT plume model, the new model (NM), the new model without pressure terms (NM-E) and the new model without the horizontal pressure term (NM-EPz). (*a–c*) Plume centreline z_c. (*d–f*) Plume radius r_m. (*g–i*) Volume flux Q. (*j–l*) Vertical momentum flux M_z.

For simulation S1, the horizontal pressure gradient is predicted remarkably well, but the prediction for the vertical pressure gradient P_z is wrong, to the extent that even the sign is incorrect. This implies that the pressure model presented here is incapable of representing plumes in weak crossflows.

7. Integral plume model

In this section, existing integral models are compared with the model having the parameterisations developed here. To be precise, the governing equations for the new model are

$$\frac{\mathrm{d}Q}{\mathrm{d}s} = \mathcal{L}, \quad \frac{\mathrm{d}M_x}{\mathrm{d}s} = -P_x, \quad \frac{\mathrm{d}M_z}{\mathrm{d}s} = -P_z + B, \quad \frac{\mathrm{d}F}{\mathrm{d}s} = 0, \tag{7.1a–d}$$

with entrainment closure ((5.1), (5.3)) and pressure closure (6.4). The coefficients used are $a = 0.9$ and $c = 0.8$. The DRWT model in (2.17) uses parameters $\alpha = 0.1$, $\beta' = 0.5$ and $n = 1.5$ and, as stated earlier, the added-mass coefficient $k = 0$. Figure 15 shows the comparison for simulations S1, S3 and S5 between the DNS data (thick black line), the DRWT model (green line), the model with new pressure and entrainment parameterisations (NM; blue line), the new model without horizontal pressure (NM-EPz; blue dashed line) and the new model without the pressure terms (NM-E; blue dash-dotted line).

The first thing to note is that z_c is much better predicted with NM than with the DRWT model for the high-crossflow cases. This is directly associated with the parameterisation of the vertical pressure term P_z. Indeed, neglecting the horizontal pressure term (NM-EPz) can be seen to have virtually the same behaviour as NM. However, upon neglecting both pressure terms (NM-E), the model behaves very similarly to the DRWT model. The fact that P_x is dynamically insignificant can be understood from the fact that it appears in the M_x equation, which represents the momentum surplus. In the integral equations M_x appears only in terms of its contribution to M_s, the integral streamwise momentum flux. Thus, it always appears in a term of the form $(QU + M_x)^{1/2}$, but $QU \gg M_x$, so the contribution from this term is dominated by QU. It is therefore unsurprising that M_x may be dynamically neglected. It should be noted that the DRWT model makes this assumption by default.

The DRWT model performs very well in terms of the evolution of r_m. The NM model can be seen to overpredict r_m for the weak-crossflow case S1, but to accurately predict r_m for the higher-crossflow cases S1 and S3. Here, it should be noted that the DRWT entrainment model uses β' as its bent-over-limit entrainment coefficient, so appropriate scaling of r_m should be expected. For the volume flux Q, the DRWT model provides accurate predictions. Surprisingly, the NM-E model – despite being able to predict the actual entrainment much more accurately than the DRWT model – severely overpredicts Q for all simulations. Once more, this highlights the importance of the pressure terms, as the inclusion of pressure (NM-EPz and NM) results in accurate predictions for S3 and S5. In the weak-crossflow case S1, the volume flux is overpredicted, demonstrating that the model needs to be augmented with a weak-crossflow parameterisation in future work.

The equation for M_z provides the key to understanding the disparities in the plume trajectories. It can be seen that M_z is dramatically overestimated by the DRWT model, as well as the NM-E model for cases S3 and S5. Since $w_m = M_z/Q$, this leads to an overestimation of the plume angle φ_u. A model for the integral vertical pressure difference over the plume (6.4), or an added-mass coefficient k, is essential in order to capture the damping effect that pressure has on the increase of vertical momentum. With the inclusion of P_z, we can see a dramatic improvement over the DRWT model for S3 and S5. Consistent with earlier observations, NM fails to predict the behaviour of the integral quantities at low flow speeds. At low U, the pressure term becomes much less significant in reducing the upwards momentum of the plume. The plume is accurately modelled by the DRWT model in the case of lower crossflow speed, so a further improvement of the model could be the amalgamation of the two models, but this is beyond the scope of this paper.

8. Range-of-validity estimate

In this section, we investigate the far-field behaviour of the new model theoretically. We will see that the far-field behaviour is not consistent with the two-thirds law in the very far

field, which allows us to provide an estimate for the rage of validity of the current model. In order to do so, we reformulate the pressure effects as an added-mass coefficient k'. Using that P_z is the dynamically dominant pressure effect, and substituting $P_z = k'\mathrm{d}M_z/\mathrm{d}s$ into the vertical momentum equation results in

$$(1+k')\frac{\mathrm{d}M_z}{\mathrm{d}s} = B, \quad k' = \frac{c\cos^2\varphi}{1-c\cos^2\varphi}, \tag{8.1a,b}$$

where we have made use of (6.4*b*). In the bent-over case, $\varphi \ll 1$, implying that $k' = c/(1-c)$ which evaluates to $k' = 4$ upon using $c = 0.8$. This value is much higher than that reported in table 1 and may be related to the fact that the plume angle, φ, does not align with the streamlines.

For a bent-over plume, $\varphi_u \ll 1$ and so (4.5) becomes

$$\frac{\mathrm{d}z_c}{\mathrm{d}x} = \frac{w_m}{U} + \theta_f \tag{8.2}$$

or alternatively $\varphi = \varphi_u + \theta_f$. Assuming that $\theta_f \ll w_m/U$, we may introduce the perturbation series

$$z_c = f_0 + \theta_f f_1 + \theta_f^2 f_2 + \cdots. \tag{8.3}$$

An analogous relationship between z_c and x to that in (2.16) can be derived following the analysis in §2.2, i.e. from the vertical momentum flux equation (2.11*c*) in the bent-over limit on making use of (8.2) and the analogous equation to (2.15) (which follows from the volume flux equation (2.11*a*) in the bent-over limit with (5.1) and (5.3)). Thus it can be shown that for $z_c \gg r_0/a$

$$f_0 = \left(\frac{3}{2}\right)^{1/3}\left(\frac{a\,\ell_b}{1+k'}\right)^{1/3}(x-x_v)^{2/3} \tag{8.4}$$

and

$$f_1 = \frac{1}{2}\left(\frac{3}{2}\right)^{2/3}\left(\frac{a\,\ell_b}{1+k'}\right)^{1/3}(x-x_v)^{2/3} + \frac{3}{7}(x-x_v). \tag{8.5}$$

Comparing the leading-order term f_0 with the linear term in f_1, linear behaviour will tend to dominate beyond the point where

$$\frac{3}{7}\theta_f\, x \sim \left(\frac{3}{2}\right)^{1/3}\left(\frac{a\,\ell_b}{1+k'}\right)^{1/3} x^{2/3}, \tag{8.6}$$

implying that the linear term will start dominating for downstream distances greater than the order

$$x/\ell_b \sim \theta_f^{-3}. \tag{8.7}$$

From the data in figure 11(*c*), it may be estimated that this distance ranges from $> 1000\ell_b$ for S5 to perhaps $> 100\ell_b$ for S1. Thus the simulations here are all in the range where the two-thirds law dominates (see figure 7*b*). Since linear behaviour is not expected in the far field, (8.7) may provide one estimate of the applicable range of this near-source model.

On neglecting the linear term in (8.5) and comparing (2.16) with the first two terms of (8.3), given by (8.4) and (8.5), respectively, we find that

$$\frac{1}{\beta^2} = \left[1 + \frac{\theta_f}{2}\left(\frac{3}{2}\right)^{1/3}\right]^3 \frac{a}{1+k'}, \tag{8.8}$$

with $\theta_f = 0.06$ (see figure 11*c*), $a = 0.9$ and $k' = 4$. This implies that the slope of r_m versus z is $\beta' = \beta/\sqrt{(1+k')} = 1.00$, which is within 20 % of the values reported in table 1 for S3–S5.

9. Conclusion

In this paper we performed a set of DNS of turbulent plumes in a crossflow for a range of Ri_U between 0.3 and 8.0, spanning strong to weak crossflows. A striking finding was that the data revealed a discrepancy between the plume trajectory, based on either the central streamline z_U or the centre of mass z_c, and the streamlines of the mean velocity averaged across the plume width. Instead, it was the field lines of the total (mean + turbulent) buoyancy flux that aligned with z_c and z_U. The plume slopes $\mathrm{d}z_c/\mathrm{d}x$ and $\mathrm{d}z_U/\mathrm{d}x$ were substantially larger than the velocity ratio $w_m/(U+u_m)$ which is typically used in integral models, implying that a correction was needed to accurately predict the plume evolution. The plume slope $\mathrm{d}z_c/\mathrm{d}x$ correlated strongly with the ratio of the total vertical to horizontal integral buoyancy flux $(F_z + F_z')/(F_x + F_x')$, and further analysis showed that the difference between $w_m/(U+u_m)$ and $(F_z + F_z')/(F_x + F_x')$ was determined by the vertical turbulent buoyancy flux.

Detailed analysis of the entrainment into the plume showed that the Leibniz terms dominate for strong crossflow plumes. Furthermore, it was shown that standard entrainment closures do not accurately represent the entrainment flux for the cases studied here and a new closure was presented. Interestingly, the DRWT plume model was able to capture the evolution of the volume flux Q better than a plume model with the new entrainment closure (NM-E), despite the development of the latter model being based on the DNS data. This firstly demonstrated that the pressure modification (added-mass term) plays an important indirect role in the entrainment, and secondly that the DRWT coefficients are tuned to account for other unrepresented terms in the integral equations (e.g. pressure).

Pressure differences across the plume play an important role in its integral behaviour. Indeed, there is a high-pressure region at the upstream side of the plume which cannot be ignored when computing momentum budgets. This high-pressure region has the effect of damping the vertical momentum flux by exerting a downward force on the plume, whilst simultaneously exerting a force in the streamwise horizontal direction. Through an analysis of the integral momentum fluxes, we showed that the downward pressure leads to a reduced vertical plume velocity and that the horizontal pressure leads to a horizontal plume velocity greater than the free-stream velocity. The horizontal pressure gradient was shown not to have a strong influence on the dynamics of the plume, consistent with classical plume theory assumptions. The model including the new entrainment parameterisation and the pressure model was able to reproduce the plume trajectories much better than existing models for sufficiently strong crossflows (essentially all values of Ri_U studied here with exception of $Ri_U = 8$ (simulation S1)).

It was shown using a perturbation expansion that the far-field behaviour of the model developed here is asymptotically not as expected (§ 8), limiting the validity of the model to ranges of $100\ell_b$–$1000\ell_b$ based on the data considered here. This incorrect far-field

behaviour is most likely caused by the entrainment parameterisation (5.2); it depends on Ri_U only, but far away from the source, the entrainment can be expected to forget about the source conditions (and therefore Ri_U) and should depend on w_m/U only.

The new integral model was constructed without any *a priori* assumptions, and all parameterisations are based on simulation data. Its value is that it reveals the physics of the problem, in particular how entrainment, turbulence and pressure influence the evolution of the plume centreline. Further work covering larger downstream domains and forced releases ($Q_0 > 0$) is needed to extend the validity of the model and its predictive capability.

Funding. We would like to acknowledge support from the Centre for Doctoral Training in Fluid Dynamics across Scales (grant number EP/L016230/1). The computational resources required to perform the simulations were provided through the UK Turbulence Consortium (grant number EP/R029326/1).

Declaration of interests. The authors report no conflict of interest.

Author ORCIDs.
Owen H. Jordan https://orcid.org/0000-0002-4443-6469;
Gabriel G. Rooney https://orcid.org/0000-0002-3787-1198;
Benjamin J. Devenish https://orcid.org/0000-0002-4071-0811;
Maarten van Reeuwijk https://orcid.org/0000-0003-4840-5050.

Appendix A. Derivation of the integral identity

The equations are all of the form

$$\boldsymbol{\nabla} \cdot \boldsymbol{F} = G, \tag{A1}$$

where $\boldsymbol{F} = \boldsymbol{u}\phi$, and $\phi(\boldsymbol{x})$, $G(\boldsymbol{x})$ are scalar functions. The position vector in the plume coordinate system (s, y, η) is given by $\boldsymbol{x} = \boldsymbol{X}(s) + \boldsymbol{e}_y y + \boldsymbol{e}_\eta(s)\eta$, where $\boldsymbol{X}(s)$ is the plume centreline and the unit vectors are given by

$$\boldsymbol{e}_s = \begin{pmatrix} \cos\varphi \\ 0 \\ \sin\varphi \end{pmatrix}, \quad \boldsymbol{e}_y = \begin{pmatrix} 0 \\ 1 \\ 0 \end{pmatrix}, \quad \boldsymbol{e}_\eta = \begin{pmatrix} -\sin\varphi \\ 0 \\ \cos\varphi \end{pmatrix}. \tag{A2a–c}$$

In the (s, y, η) system, the divergence becomes

$$\boldsymbol{\nabla} \cdot \boldsymbol{F} = \frac{1}{1 - \eta \dfrac{\mathrm{d}\varphi}{\mathrm{d}s}} \left(\frac{\partial F_s}{\partial s} + \frac{\partial F_\eta}{\partial \eta} \right) + \frac{\partial F_y}{\partial y}, \tag{A3}$$

where the streamwise and normal fluxes are defined, respectively, as

$$F_s = F_x \cos\varphi + F_z \sin\varphi, \tag{A4a}$$

$$F_\eta = (-F_x \sin\varphi + F_z \cos\varphi) \left(1 - \eta \frac{\mathrm{d}\varphi}{\mathrm{d}s} \right). \tag{A4b}$$

Since curvature effects will only be important very close to the source, it is assumed that $\eta\, \mathrm{d}\varphi/\mathrm{d}s \ll 1$. This assumption can be justified by invoking theory for bent-over plumes. Indeed, assuming that the edge of the plume is at $\eta \sim r$, and using ((2.15), (2.16)), we have $\eta \propto x^{2/3}$. For bent-over plumes, the small-angle assumption $\tan\varphi \approx \varphi$ holds, which implies that $\varphi \approx \mathrm{d}z_c/\mathrm{d}x$. Since $z_c \propto x^{2/3}$, it follows that $\varphi \propto x^{-1/3}$. Once more invoking the small-angle assumption to note that $\mathrm{d}\varphi/\mathrm{d}s \approx \mathrm{d}\varphi/\mathrm{d}x$, we find that $\mathrm{d}\varphi/\mathrm{d}s \propto x^{-4/3}$ and

thus that $\eta\,\mathrm{d}\varphi/\mathrm{d}s \sim x^{-2/3}$. This implies that this term can be ignored a few radii downstream of the source. With this simplification, the Jacobian $1 - \eta\,\mathrm{d}\varphi/\mathrm{d}s \approx 1$.

Integration of (A1) over the plume area, whose domain is denoted Ω, expressed in the (s, y, η) coordinate system results in (using identity (2.5) for a steady state ($\boldsymbol{v} = 0$) from van Reeuwijk *et al.* (2021))

$$\frac{\mathrm{d}}{\mathrm{d}s}\iint_{\Omega} u_s\phi\,\mathrm{d}A = \oint_{\partial\Omega} u_s\phi\frac{N_s}{|\boldsymbol{N}_\perp|}\,\mathrm{d}\ell + \oint_{\partial\Omega} \boldsymbol{u}_\perp\phi\cdot\boldsymbol{n}\,\mathrm{d}\ell + \iint_{\Omega} G\,\mathrm{d}A, \tag{A5}$$

where the first and second terms on the right-hand side of the equation are the Leibniz and radial contributions to entrainment, respectively. Here, $\boldsymbol{N} = (N_s, N_y, N_\eta)^{\mathrm{T}}$ denotes the three-dimensional inward-pointing normal along the plume boundary $\partial\Omega$, $\boldsymbol{N}_\perp = (N_y, N_\eta)^{\mathrm{T}}$ and $\boldsymbol{u}_\perp = (u_y, u_\eta)^{\mathrm{T}}$ are the vector components in the (y, η) plane and $\boldsymbol{n} = \boldsymbol{N}_\perp/|\boldsymbol{N}_\perp|$ is the two-dimensional normal in the (y, η) plane.

References

Briggs, G.A. 1982 Plume rise predictions. In *Lectures on Air Pollution and Environmental Impact Analyses* (ed. D.A. Haugen), pp. 59–111. American Meteorological Society.

Briggs, G.A. 1984 *Plume Rise and Buoyancy Effects*, chap. *8*, pp. 325–364. Office of Research. US Department of Energy.

Cintolesi, C., Petronio, A. & Armenio, V. 2019 Turbulent structure of buoyant jet in cross-flow studied through large-eddy simulation. *Environ. Fluid Mech.* **19**, 401–433.

Contini, D., Donateo, A., Cesari, D. & Robins, A.G. 2011 Comparison of plume rise models against water tank experimental data for neutral and stable crossflows. *J. Wind Engng Ind. Aerodyn.* **99** (5), 539–553.

Costa, A., *et al.*2016 Results of the eruptive column model inter-comparison study. *J. Volcanol. Geotherm. Res.* **326**, 2–25.

Craske, J. & van Reeuwijk, M. 2015 Energy dispersion in turbulent jets. Part 1. Direct simulation of steady and unsteady jets. *J. Fluid Mech.* **763**, 500–537.

Davidson, G.A. 1989 Simultaneous trajectory and dilution predictions from a simple integral plume model. *Atmos. Environ.* **23** (2), 341–349.

De Wit, L., Van Rhee, C. & Keetels, G. 2014 Turbulent interaction of a buoyant jet with cross-flow. *ASCE J. Hydraul. Engng* **140** (12), 04014060.

Devenish, B.J. 2013 Using simple plume models to refine the source mass flux of volcanic eruptions according to atmospheric conditions. *J. Volcanol. Geotherm. Res.* **256**, 118–127.

Devenish, B.J., Rooney, G.G., Webster, H.N. & Thomson, D.J. 2010 The entrainment rate for buoyant plumes in a crossflow. *Boundary-Layer Meteorol.* **134** (3), 411–439.

Fan, L.-N. 1967 Turbulent buoyant jets into stratified or flowing ambient fluids. PhD thesis, CalTech.

Fischer, H.B., Koh, R.C.Y., Imberger, J. & Brooks, N.H. 1979 *Mixing in Inland and Coastal Waters*. Academic Press.

Frölich, J., Denev, J.A. & Bockhorn, H. 2004 Large eddy simulation of a jet in crossflow. In *European Congress on Computational Methods in Applied Sciences and Engineering* (ed. P. Neittaanmaki, T. Rossi, K. Majava & O. Pironneau).

Gaskin, S.J. 1995 Single buoyant jets in a crossflow and the advected line thermal. PhD thesis, University of Canterbury.

Hewett, T.A., Fay, J.A. & Hoult, D.P. 1971 Laboratory experiments of smokestack plumes in a stable atmosphere. *Atmos. Environ.* **5** (9), 767–789.

Hoult, D.P. & Weil, J.C. 1972 Turbulent plume in a laminar cross flow. *Atmos. Environ.* **6** (8), 513IN1531–530.

Hunt, G.R. & Kaye, N.B. 2005 Lazy plumes. *J. Fluid Mech.* **533**, 329–338.

Huq, P. & Dhanak, M.R. 1996 The bifurcation of circular jets in crossflow. *Phys. Fluids* **8** (3), 754–763.

Huq, P. & Stewart, E.J. 1996 A laboratory study of buoyant plumes in laminar and turbulent crossflows. *Atmos. Environ.* **30** (7), 1125–1135.

Huq, P. & Stewart, E.J. 1997 Measurements of density fluctuations in steady, buoyant plumes in crossflow. *Atmos. Environ.* **31** (11), 1677–1688.

Jordan, O.H. 2021 Turbulent plumes in a uniform crosswind. MPhil thesis, Imperial College London.

LEE, J.H.W. & CHU, V.H. 2003 *Turbulent Jets and Plumes: A Lagrangian Approach*. Kluwer.
LIST, E.J. 1982 Turbulent jets and plumes. *Annu. Rev. Fluid Mech.* **14** (1), 189–212.
MAHESH, K. 2013 The interaction of jets with cross-flow. *Annu. Rev. Fluid Mech.* **45**, 379–407.
MORTON, B.R., TAYLOR, G. & TURNER, J.S. 1956 Turbulent gravitational convection from maintained and instantaneous sources. *Proc. R. Soc. Lond.* A **234** (1196), 1–23.
MUPPIDI, S. & MAHESH, K. 2005 Study of trajectories of jets in crossflow using direct numerical simulations. *J. Fluid Mech.* **530**, 81–100.
MUPPIDI, S. & MAHESH, K. 2006 Two-dimensional model problem to explain counter-rotating vortex pair formation in a transverse jet. *Phys. Fluids* **18**, 085103.
POPE, S.B. 2000 *Turbulent Flows*. Cambridge University Press.
PRIESTLEY, C.H.B. & BALL, F.K. 1955 Continuous convection from an isolated source of heat. *Q. J. R. Meteorol. Soc.* **81** (348), 144–157.
VAN REEUWIJK, M. & CRASKE, J. 2015 Energy-consistent entrainment relations for jets and plumes. *J. Fluid Mech.* **782**, 333–355.
VAN REEUWIJK, M., SALIZZONI, P., HUNT, G.R. & CRASKE, J. 2016 Turbulent transport and entrainment in jets and plumes: a DNS study. *Phys. Rev. Fluids* **1** (7), 074301.
VAN REEUWIJK, M., VASSILICOS, J.C. & CRASKE, J. 2021 Unified description of turbulent entrainment. *J. Fluid Mech.* **908**, A12.
ROONEY, G.G. 2015 Merging of a row of plumes or jets with an application to plume rise in a channel. *J. Fluid Mech.* **771**, R1.
ROSSI, E., BONADONNA, C. & DEGRUYTER, W. 2019 A new strategy for the estimation of plume height from clast dispersal in various atmospheric and eruptive conditions. *Earth Planet Sci. Lett.* **505**, 1–12.
SCHATZMANN, M. 1978 The integral equations for round buoyant jets in stratified flows. *Z. Angew. Math. Phys.* **29** (4), 608–630.
STEVENS, R.J.A.M., GRAHAM, J. & MENEVEAU, C. 2014 A concurrent precursor inflow method for Large Eddy Simulations and applications to finite length wind farms. *Renew. Energy* **68**, 46–50.
WEIL, J.C. 1988 Plume rise. In *Lectures on Air Pollution Modeling* (ed. A. Venkatram & J.C. Wyngaard), pp. 119–166. American Meteorological Society.
WOODHOUSE, M.J., HOGG, A.J., PHILLIPS, J.C. & SPARKS, R.S.J. 2013 Interaction between volcanic plumes and wind during the 2010 Eyjafjallajökull eruption, Iceland. *J. Geophys. Res.* **118** (1), 92–109.
WOODS, A.W. 2010 Turbulent plumes in nature. *Annu. Rev. Fluid Mech.* **42**, 391–412.
YUAN, L.L., STREET, R.L. & FERZIGER, J.H. 1999 Large-eddy simulations of a round jet in crossflow. *J. Fluid Mech.* **379**, 71–104.
YUAN, L.L. & STREET, R.L. 1998 Trajectory and entrainment of a round jet in crossflow. *Phys. Fluids* **10**, 2323.